Electronic Supplementary Material (ESI) for Energy & Environmental Science.

Supporting information

Xuezhong Zhang[1], Zijian Dai[1], Jie Chen[1], Xin Chen[1], Xiong Lin[1], Shuang Yang[1], Kai Wu[1], Qiang Fu[1*], Hua Deng[1*]

[1]College of Polymer Science and Engineering, State Key Laboratory of Polymer Materials Engineering, Sichuan University, Chengdu 610065, PR China

Corresponding authors: huadeng@scu.edu.cn (H. Deng), qiangfu@scu.edu.cn (Q. Fu)

Table of Contents

1. Experimental Section

1.1. Materials

CS, CNF and PVA are provided by Aladdin Reagent (Shanghai) Co., Ltd. Hydrochloric acid (HCl, 37%), potassium hydroxide (KOH), hydrochloric acid (HCl, 37%), tert-butanol (TBA) and glutaraldehyde (50% aqueous solution) are supplied by Chengdu Kelong Chemical Reagent Company (China). SWNT is purchased from Deyang Carbonene Technology Co., Ltd (China). 1-carboxyethyl-3-methylimidazolium nitrate (COOH-IL) and 1-(3-aminopropyl)-3-methylimidazolium bromide (IL-NH_2) are purchased from Lanzhou Institute of Chemical Physics.

1.2. Synthesis of CSWNT and NSWNT

Firstly, 500 mL deionized water, 250 mg COOH-IL, 250 mg SWNT and 250 mg KOH were added to a 1000 mL flask and sonicated at 300 W for 30 min. Subsequently, the suspension was stirred at 90 °C for 24 h. The carboxylated single-walled carbon nanotubes (CSWNT) were obtained by washing and centrifuging the reacted suspension. Similarly, amino-functionalized single-walled carbon nanotubes (NSWNT) were also prepared using the method mentioned above.

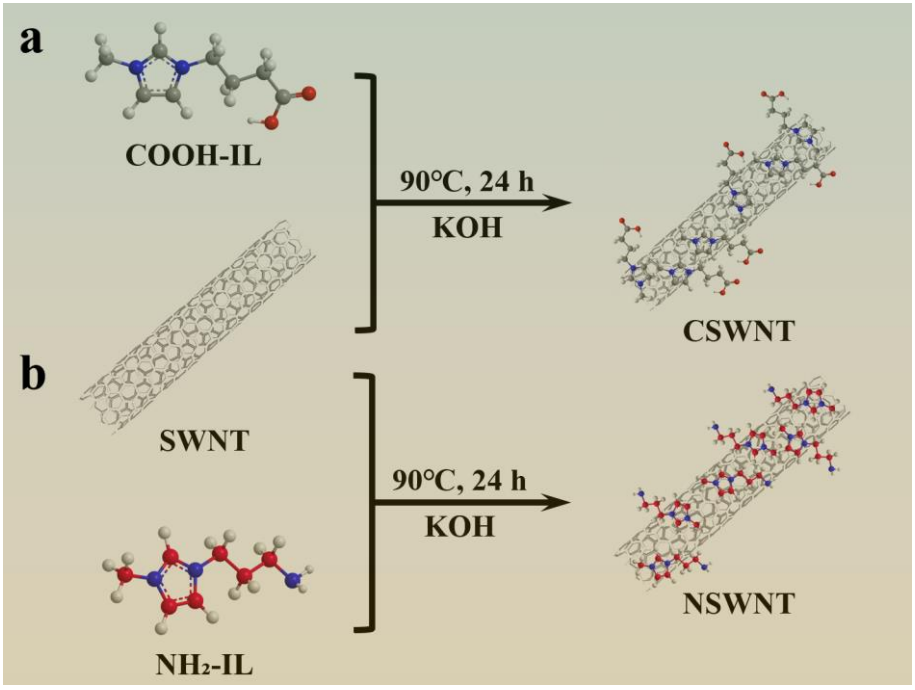

Fig. S1 The schematic diagram of a CSWNT and b NSWNT preparation

1.3. Preparation of polymer dendritic colloids

PVA dendritic colloids were obtained by slowly adding 20 g 10 wt% PVA water solution into the turbulent flow of 80 g TBA, which was formed by high-speed shearing of TBA in the IKA Magic Lab device (IKA Works Inc.) operating at 20000 rpm. CNF dendritic colloids were obtained by slowly adding 40 g 4.5 wt% CNF water solution into the turbulent flow of 50 g TBA. CS dendritic colloids were obtained by slowly adding 40 g 5 wt% CNF water solution into the turbulent flow of 60 g TBA.

1.4. Preparation of aerogels

1.4.1. Preparation of SWNT/PVA/CNF aerogels

From Fig. S2a, 1.5 g PVA particles, 50 g 1 wt% CNF solution and 48.5 mL deionized water were added to a 250 mL single-necked bottle, and the PVA/CNF solution with a mass fraction of 2 wt % was obtained by heating and stirring at 60°C. Subsequently, ultrasonication disperses SWNT in 2 wt% PVA/CNF water solution (300W, 10 min). Next, glutaraldehyde (80**μL**, 50 wt%

in DI water) and hydrochloric acid (800mL, 3 wt%) were loaded into SWNT/PVA/CNF solution (10 mL, 25mg/mL) and transferred to liquid nitrogen for freezing. Finally, after the GO/PVA was solidified, it was lyophilized in a freeze-dryer (−50°C, 10Pa).

1.4.2. Preparation of SWNT@PVA/CNF aerogels

From Fig. S2b, PVA/CNF dendritic colloids were obtained by mixing 30 g 2wt % PVA dendritic colloid and 10 g 2wt % CNF dendritic colloid. Subsequently, ultrasonication disperses SWNT in 2 wt% PVA/CNF dendritic colloids (300W, 10 min). Next, glutaraldehyde (80 μL, 50 wt% in DI water) and hydrochloric acid (800mL, 3 wt%) were loaded into SWNT/PVA/CNF dendritic colloids (10 mL, 25mg/mL) and transferred to liquid nitrogen for freezing. Finally, after the GO/PVA was solidified, it was lyophilized in a freeze-dryer (-50°C, 10Pa).

1.4.3. Preparation of NSC@PVA/CNF aerogels

From Fig. S2c, PVA/CNF dendritic colloids were obtained by mixing 30 g 2wt % PVA dendritic colloid and 10 g 2wt % CNF dendritic colloid. Subsequently, CSWNT, SWNT and NSWNT were ultrasonically dispersed into PVA/CNF, dendritic colloids to obtain CSWNT@PVA/CNF, SWNT@PVA/CNF and NSWNT@PVA/CNF dendritic colloids (300W, 10 min). Next, glutaraldehyde (80μL, 50 wt% in DI water) and hydrochloric acid (800mL, 3 wt%) were loaded to CSWNT@PVA/CNF, SWNT@CS/CNF and NSWNT@CS dendritic colloids and transferred to -20°C freezers and kept for 24h. Finally, after the dendritic colloids were solidified, they were lyophilized in a freeze-dryer (-50°C, 10Pa).

1.4.4. Preparation of SWNT@CCP aerogels

From Fig. S2d, CS/CNF dendritic colloids were obtained by mixing 30 g 2wt % CS dendritic colloid and 10 g 2wt % CNF dendritic colloid. Subsequently, SWNT were ultrasonically dispersed into PVA/CNF, CS/CNF and CS dendritic colloids to obtain SWNT@PVA/CNF, SWNT@CS/CNF and SWNT@CS dendritic colloids (300W, 10 min).

Next, glutaraldehyde (80μL, 50 wt% in DI water) and hydrochloric acid (800mL, 3 wt%) were loaded to CSWNT@PVA/CNF, SWNT@CS/CNF and NSWNT@CS dendritic colloids and transferred to -20°C freezers and kept for 24h. Finally, after the dendritic colloids were solidified, they were lyophilized in a freeze-dryer (-50°C, 10Pa).

1.4.5. Preparation of NSC@CCP aerogels

From Fig. S2e, CS/CNF dendritic colloids were obtained by mixing 30 g 2wt % CS dendritic colloid and 10 g 2wt % CNF dendritic colloid. Subsequently, CSWNT, SWNT and NSWNT were ultrasonically dispersed into PVA/CNF, CS/CNF and CS dendritic colloids to obtain CSWNT@PVA/CNF, SWNT@CS/CNF and NSWNT@CS dendritic colloids (300W, 10 min). Next, glutaraldehyde (80**μL**, 50 wt% in DI water) and hydrochloric acid (800mL, 3 wt%) were loaded to CSWNT@PVA/CNF, SWNT@CS/CNF and NSWNT@CS dendritic colloids and transferred to -20°C freezers and kept for 24h. Finally, after the dendritic colloids were solidified, they were lyophilized in a freeze-dryer (-50°C, 10Pa).

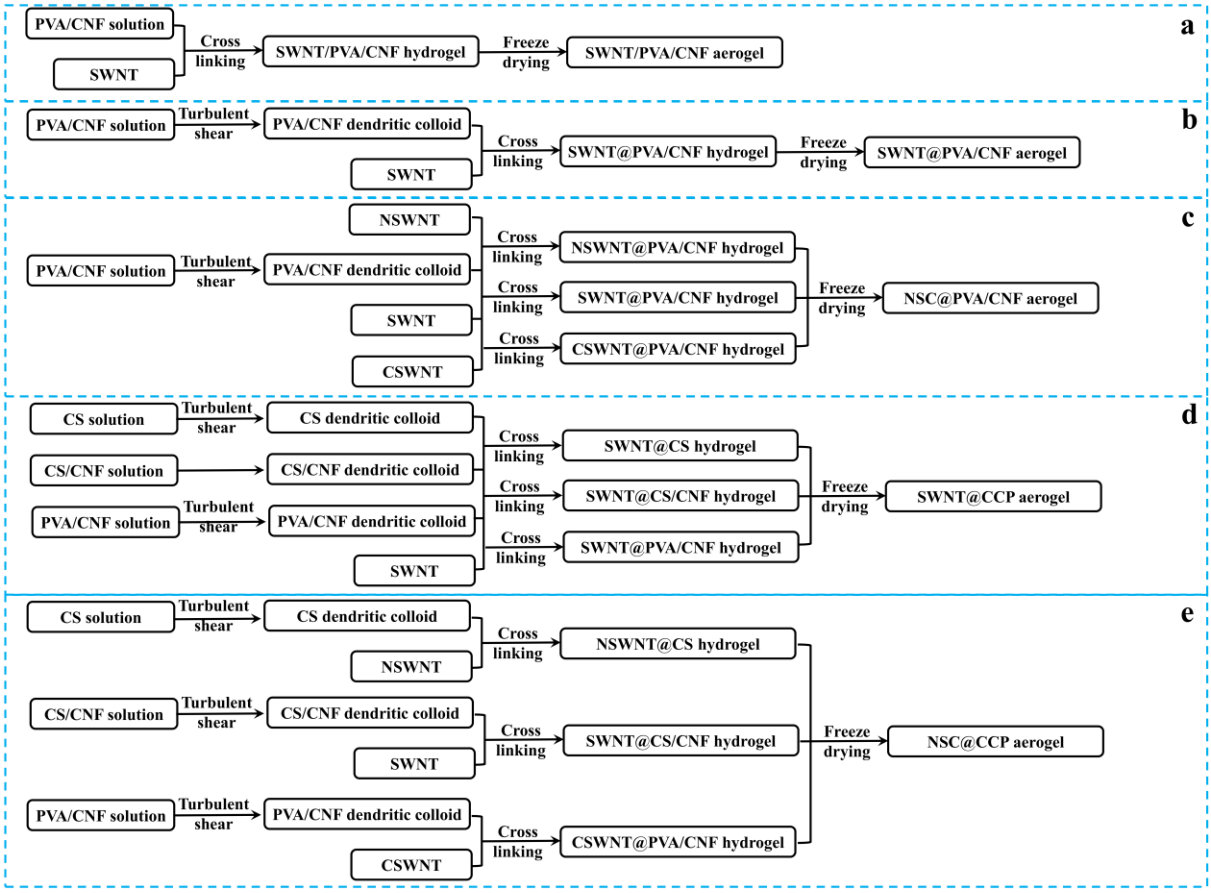

Fig. S2 Preparation diagram of composite aerogels

1.5. Preparation of MEGs

A conductive silver paste was applied to both ends of the aerogel to connect the electrode and the porous metal foam (Ni, Ag, and Pt), as is shown in Fig. S3.

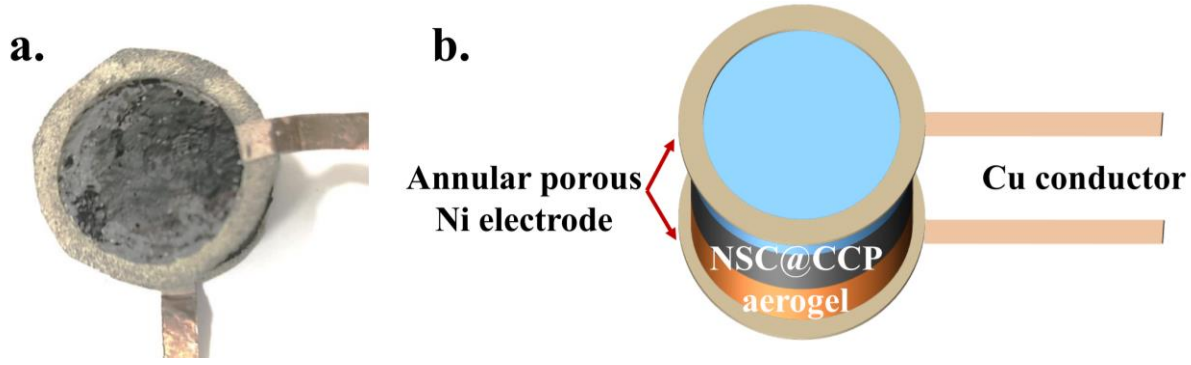

Fig. S3 a. Photograph of MEGs, b. Schematic diagram of MEGs.

2. Preparation of CSWNT and NSWNT

2.1. TEM

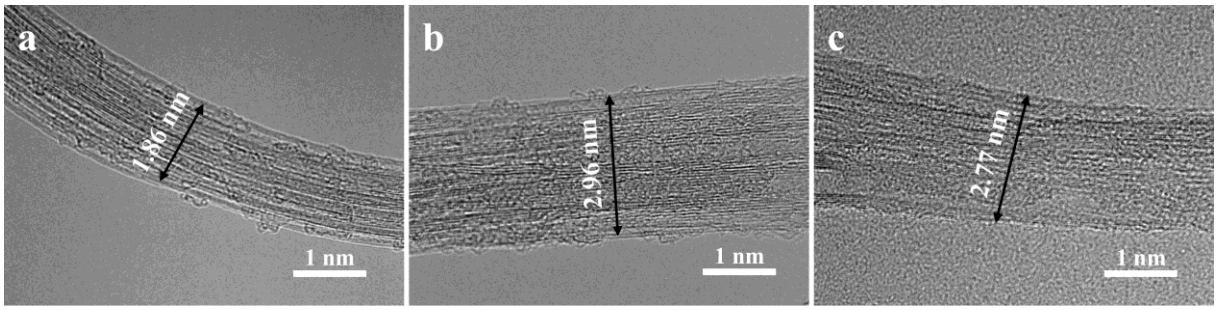

Fig. S4 (a-c) TEM of SWNT, CSWNT and NSWNT

2.2. XPS

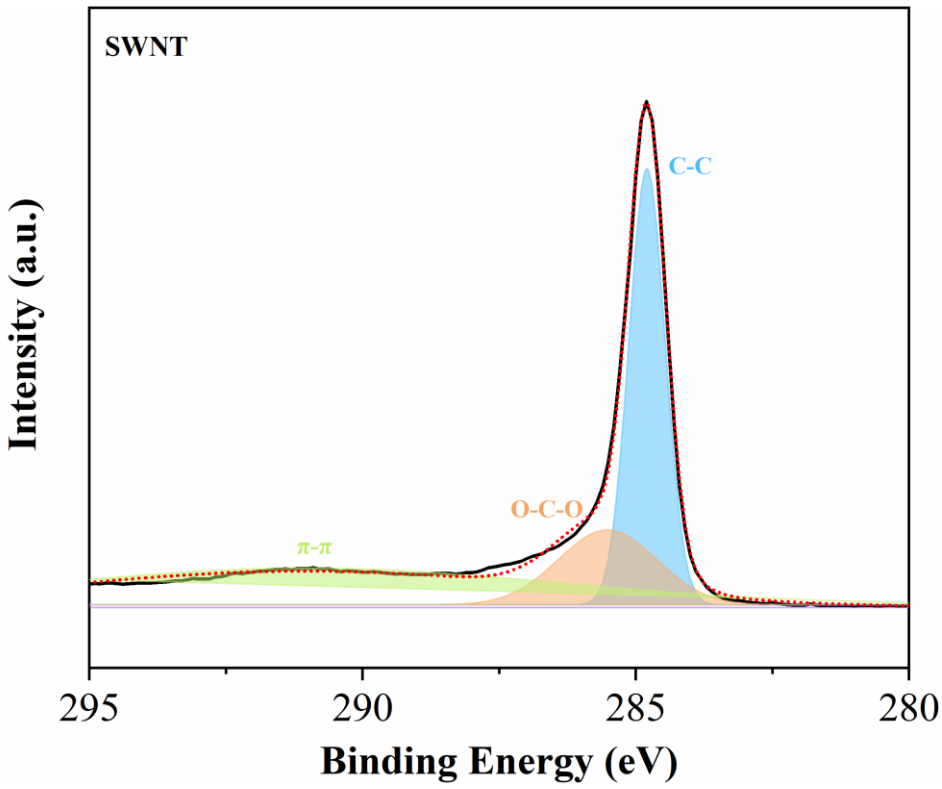

Fig. S5 C1s of SWNT

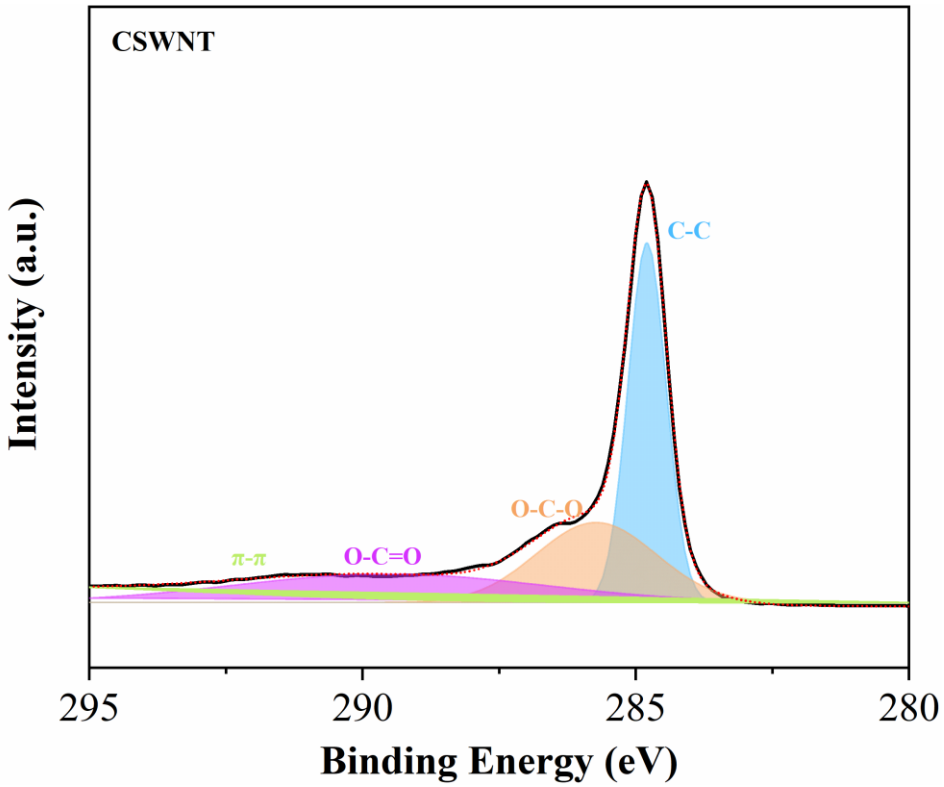

Fig. S6 C1s of CSWNT

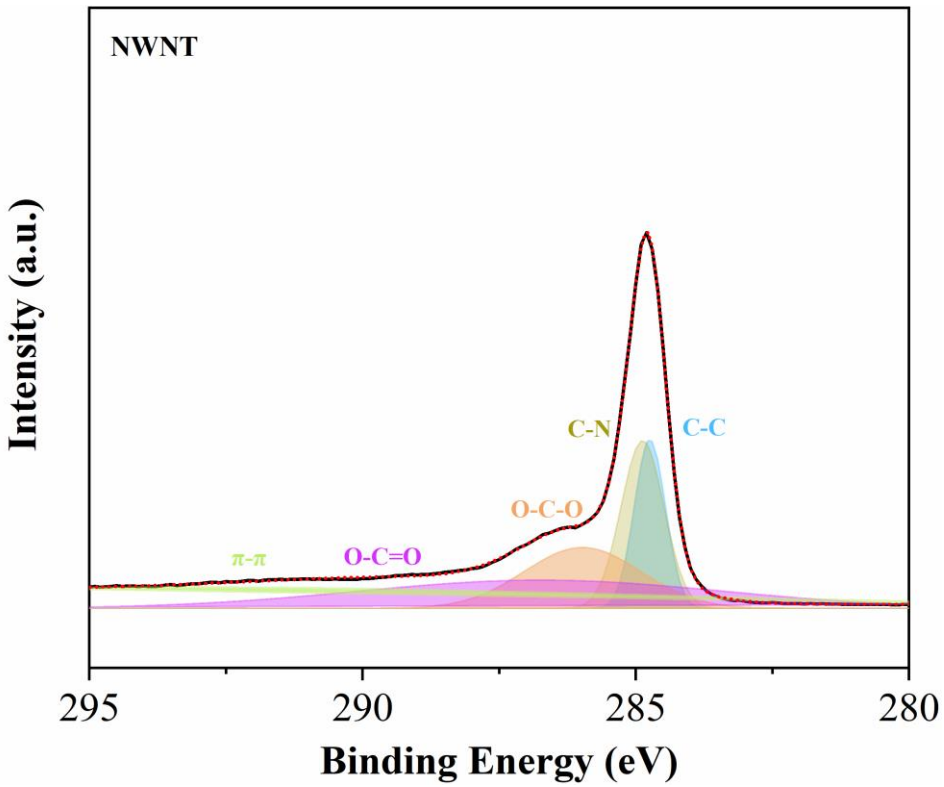

Fig. S7 C1s of NSWNT

Table S1. The mass fractions of C, N and O elements in SWNT before and after modification.

Samples	C (wt. %)	N (wt. %)	O (wt. %)
SWNT	92.72	0.76	6.52
CSWNT	70.61	5.14	24.25
NSWNT	65.86	11.82	22.32

2.3. XRD

For the original SWNT, a sharp diffraction peak of (002) crystal plane appears at 2θ = 26.4 °. According to the Bragg equation, the interplanar spacing (d) of SWNT can be calculated.

$$2d\ sin\theta\ =\ n\lambda$$

Among them, d is the interplanar spacing, θ is the angle between the incident X-ray and the corresponding crystal plane, λ is the wavelength of the X-ray, and n is the diffraction series. After calculation, the interplanar spacing d of SWNT is 3.363 Å, which is still far from the d value (3.354 Å) of graphite single crystal, which means that the graphene layer in SWNT is a disordered layer structure.

Due to the grafting of ionic liquids, the crystallization peak appears to shift to the left, the intensity decreases and the width increases. Among them, CSWNT and NSWNT have wide (002) crystal plane diffraction peaks at 2θ of 25.4° and 25.7°, respectively. The crystal plane spacing d of CSWNT and NSWNT is 3.494 and 3.454 Å, respectively, and the spacing of the graphite layer in SWNT is improved.

Table S2. Interplanar spacing of SWNT, CSWNT and NSWNT

Samples	2θ (°)	d (Å)
SWNT	26.4	3.363
CSWNT	25.4	3.494
NSWNT	25.7	3.454

2.4. Zeta potential

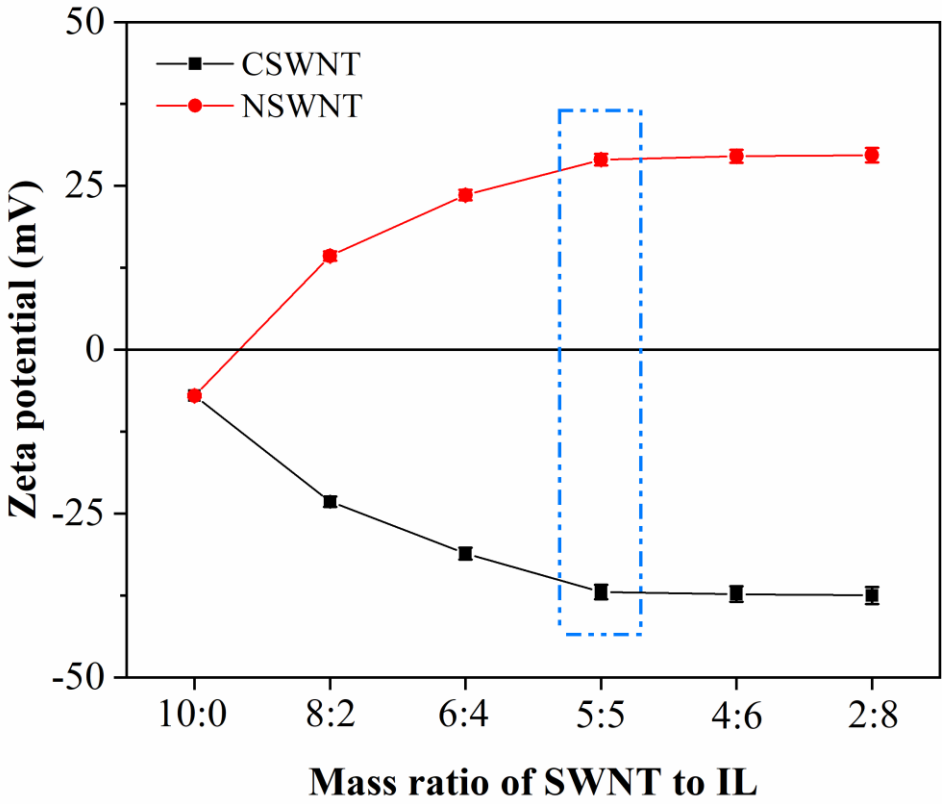

Fig. S8 Zeta potential of fillers under different mass ratios of SWNT and IL

2.5. Conductivity

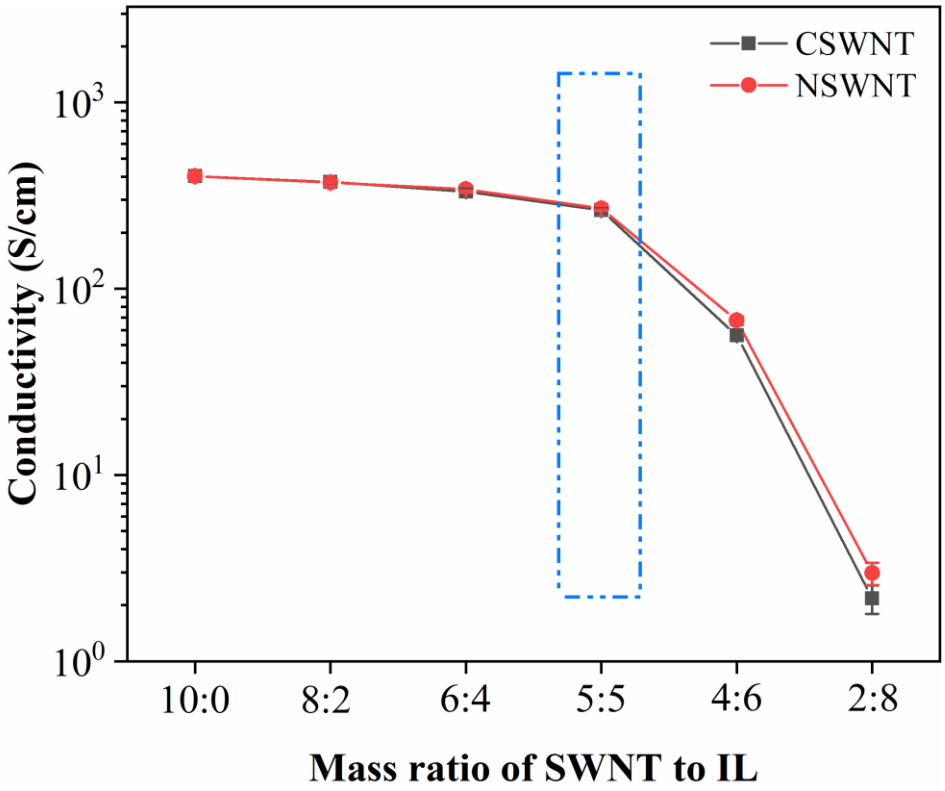

Fig. S9 The conductivity of fillers under different mass ratios of SWNT and IL

3. Characterization of dendritic colloids

3.1. Polarizing microscope

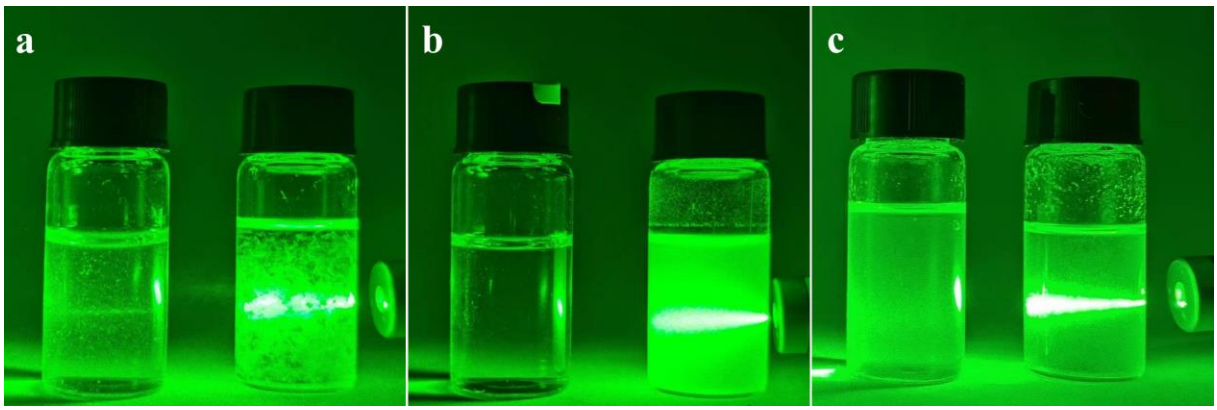

Fig. S10 Photos of the 'Tyndall' effect of polymer dendritic colloids: (a) PVA, (b) CNF and (c) CS

3.2. FESEM

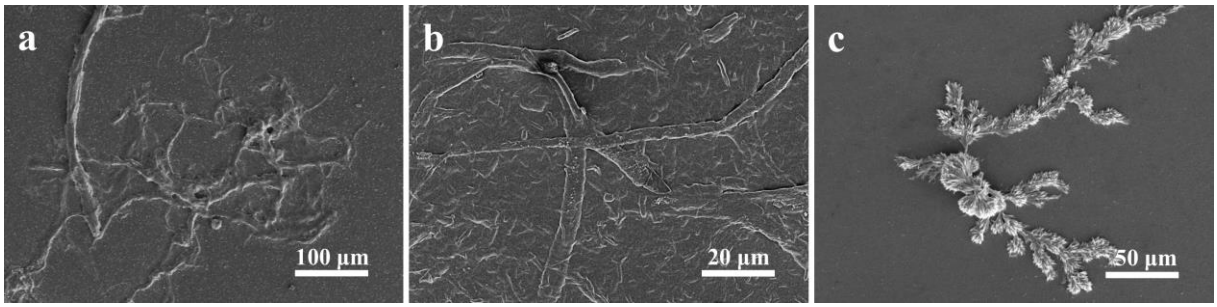

Fig. S11 FESEM of polymer dendritic colloids: (a) PVA, (b) CNF, (c) CS

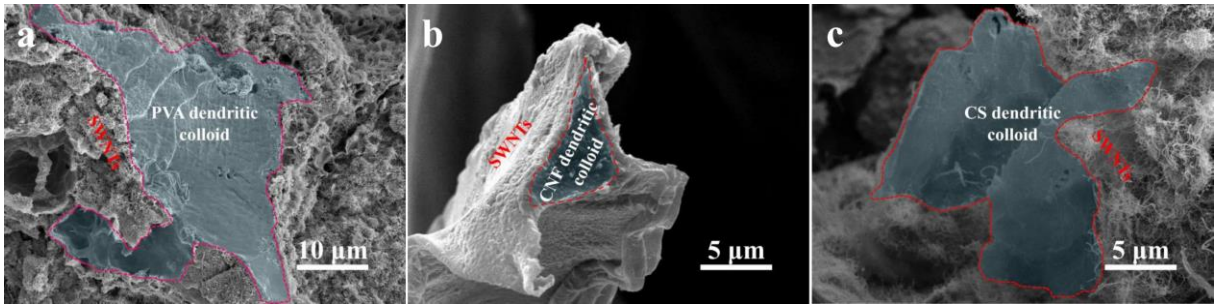

Fig. S12 FESEM of filler@polymer dendritic colloid: (a) SWNT@PVA, (b) SWNT@CNF and (c) SWNT@CS

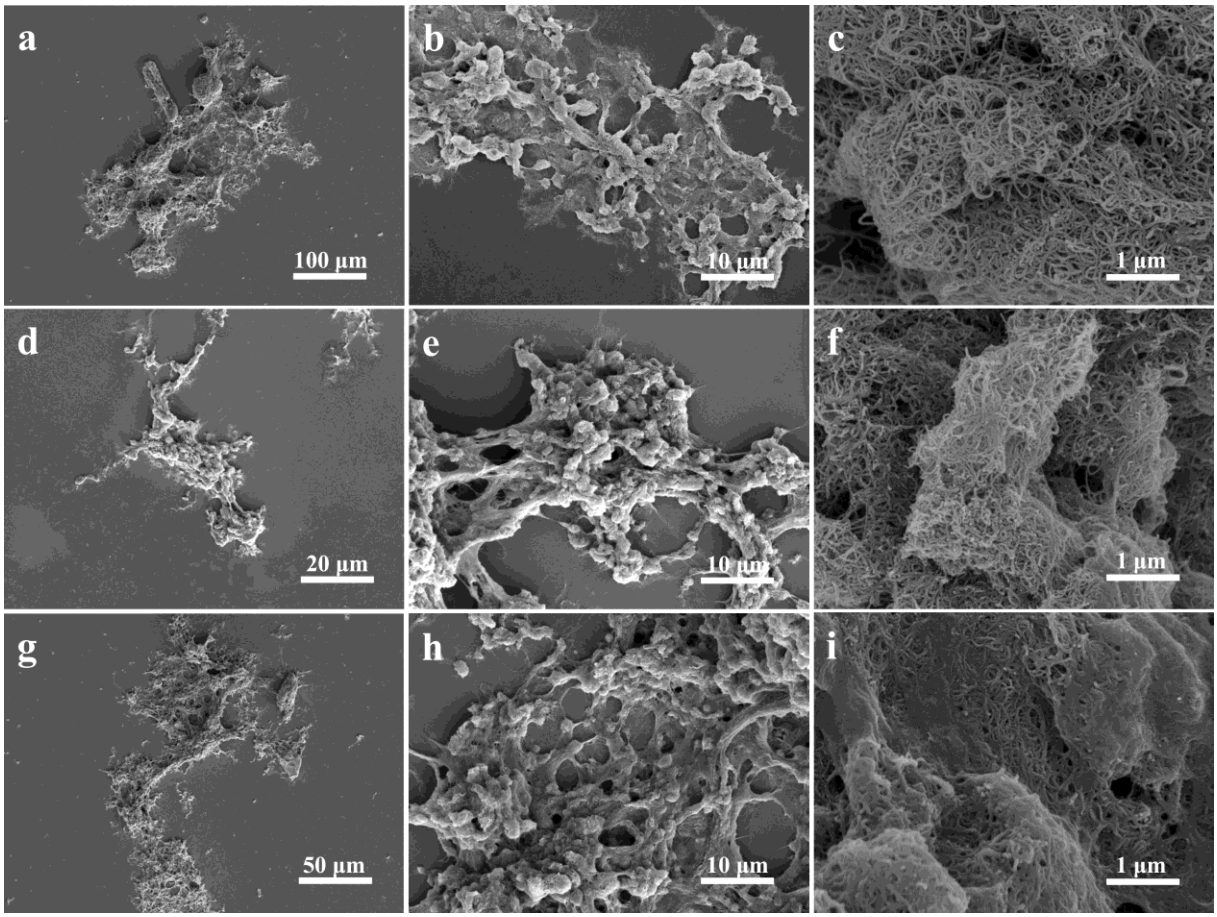

Fig. S13 FESEM of filler@polymer dendritic colloid: (a-c) CSWNT@PVA/CNF, (d-f) SWNT@CS/CNF and (g-i) NSWNT@CS

3.3. Zeta potential

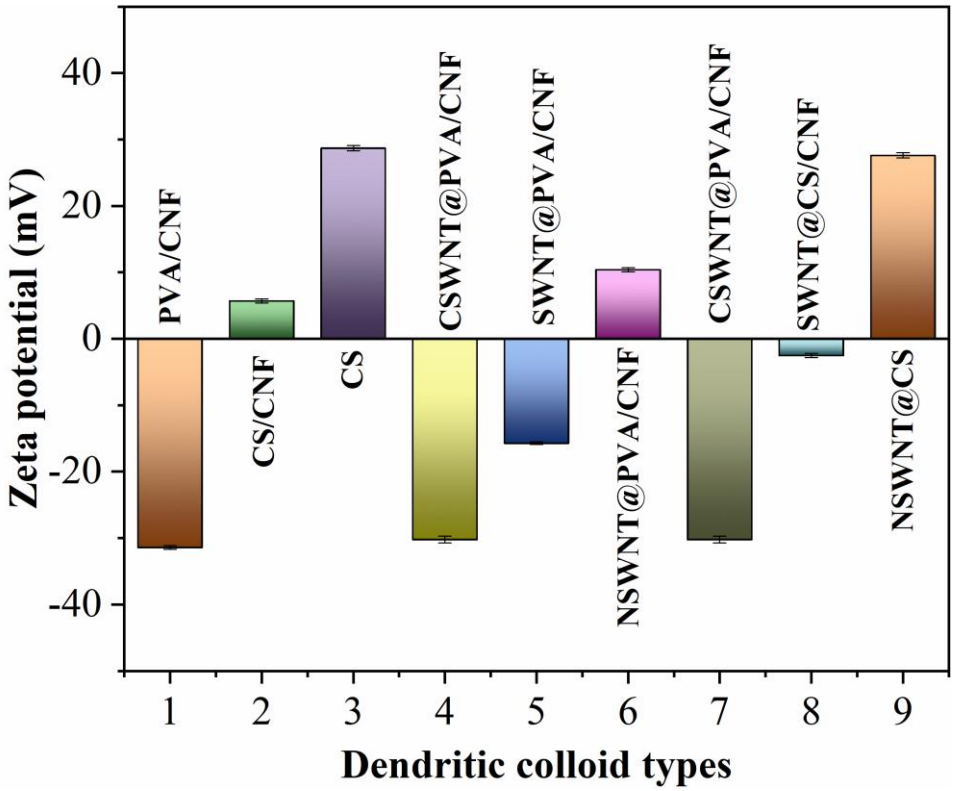

Fig. S14 Zeta potential of filler@polymer dendritic colloid

3.4. Rheology behaviour

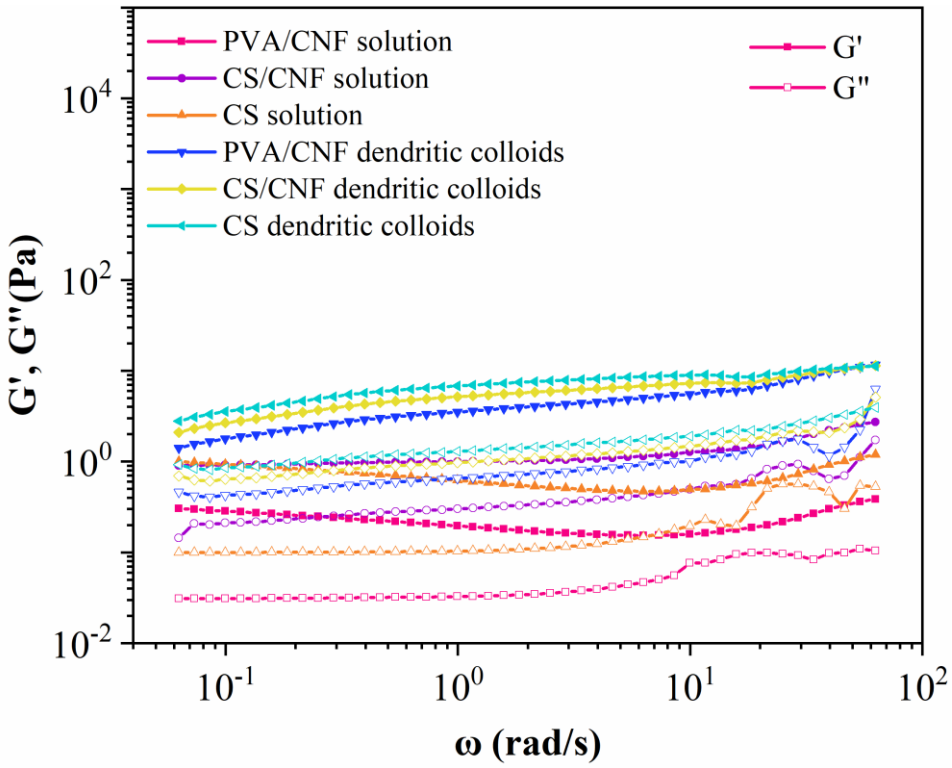

Fig. S15 Rheological behavior of polymer solution and dendritic colloid

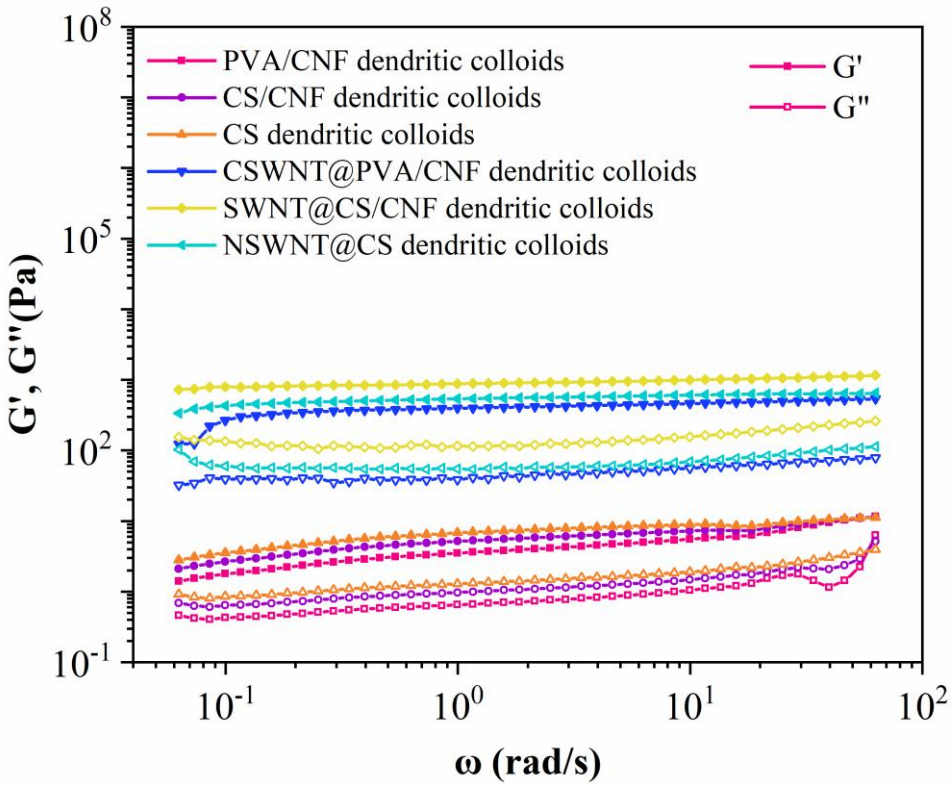

Fig. S16 Rheological behavior of Filler@dendritic colloid

4. Characterization of aerogel

4.1. BET

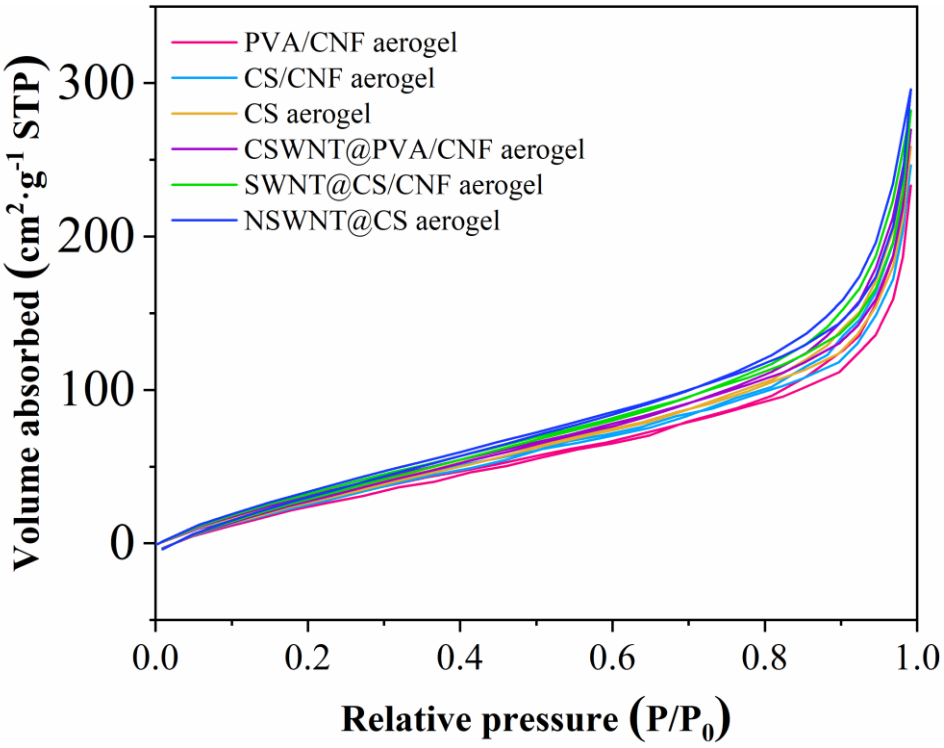

Fig. S17 The specific surface area of aerogel

4.2. Conductivity

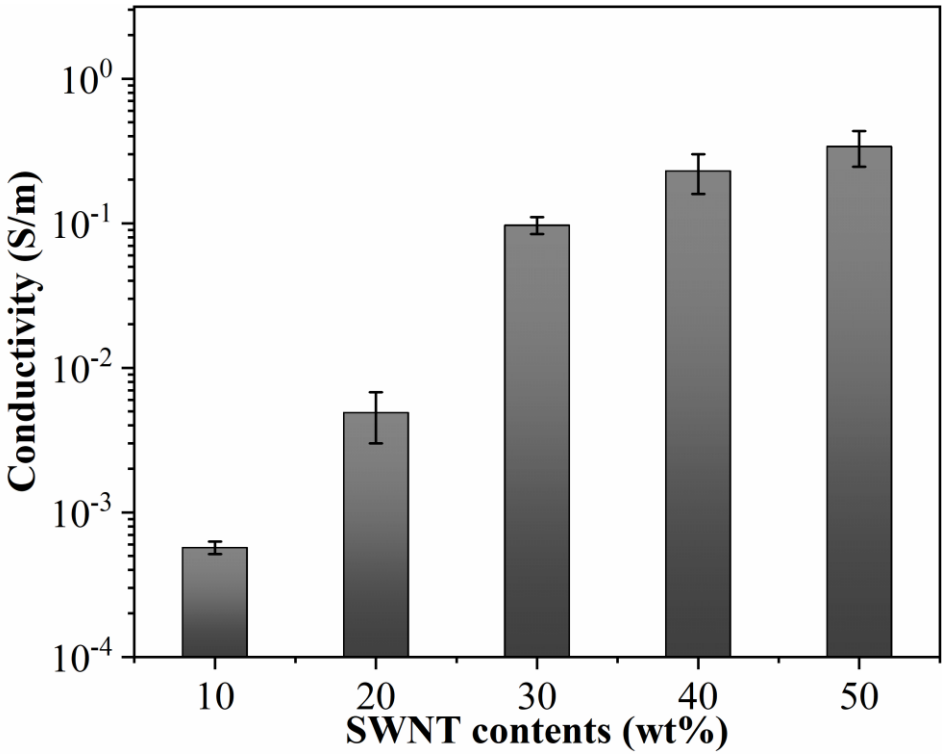

Fig. S18 The conductivity of aerogels with different SWNT contents

4.3. FESEM

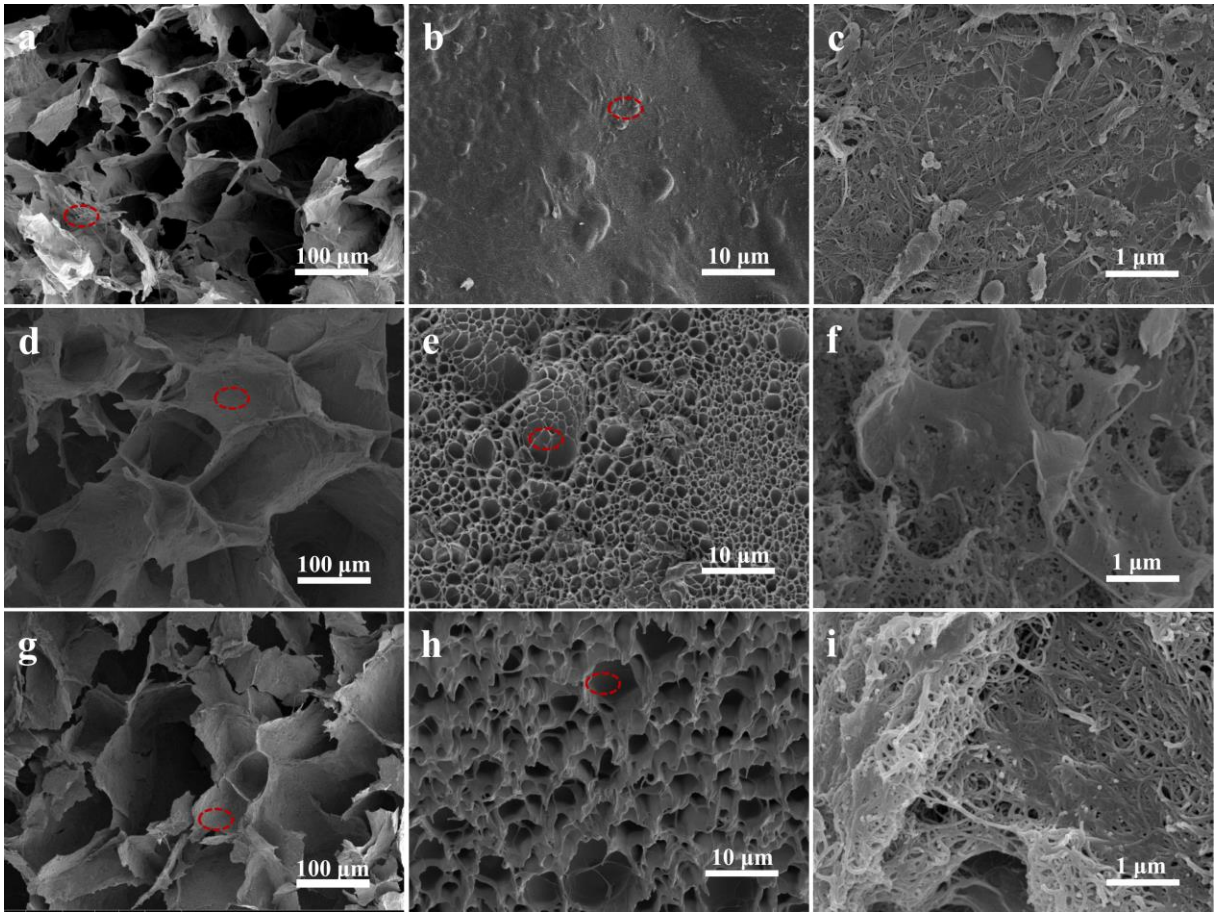

Fig. S19 FESEM of NSC@CPP aerogels: (a-c) hygroscopic layer, (d-f) medial layer, (g-i) evaporative layer.

4.4. Density and pore size

From Table S3, the density of different layers was calculated by the drainage method. The density between different aerogel layers was close, about 20 mg·cm^{-3}. In addition, BET studied the pore size of different regions of the aerogel. The aerogel includes macropores and micropores, and their diameters are about 100-200 μm and 20-30 μm. A continuous porous structure is found in the internal structure of the aerogel based on the test results of density and pore size, and determining the internal gradient structure is entirely dependent upon the surface characteristics of the material, which are independent of its density and pore size.

Table S3. Density and pore size of NSC@CPP aerogels

Samples	Density ($mg \cdot cm^{-3}$)	Pore size (μm)	
		large pores	tiny pores
hygroscopic layer	19.8 ± 0.37	147 ± 52	24 ± 16
medial layer	20.3 ± 0.41	123 ± 37	22 ± 13
evaporative layer	20.1 ± 0.49	155 ± 46	27 ± 12

4.5. Moisture-induced electricity performance

4.5.1. Content dependence

On one hand, increased SWNT content increases the probability of SWNTs contacting water molecules, the interaction between these molecules increases, and therefore, the output power of MEGs will be considerably increased. On the other hand, since the total weight of the composite airgel remains unchanged, as SWNT content increases, the amount of polymer matrix decreases, and the water absorption capacity of the airgel decreases accordingly (Fig. S20). SWNT content of 40 wt. % ultimately results in the best overall output of airgel as a result of competition between these two components (as is shown in Fig. S21-22).

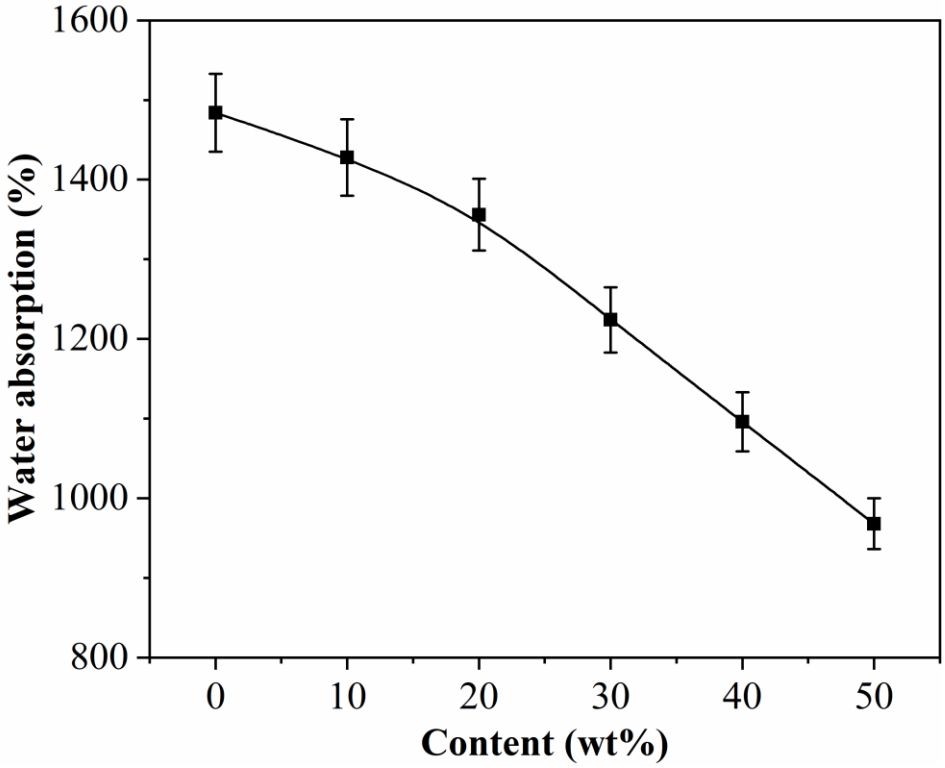

Fig. S20 Water absorption of SWNT/PVA/CNF aerogels with different SWNT contents

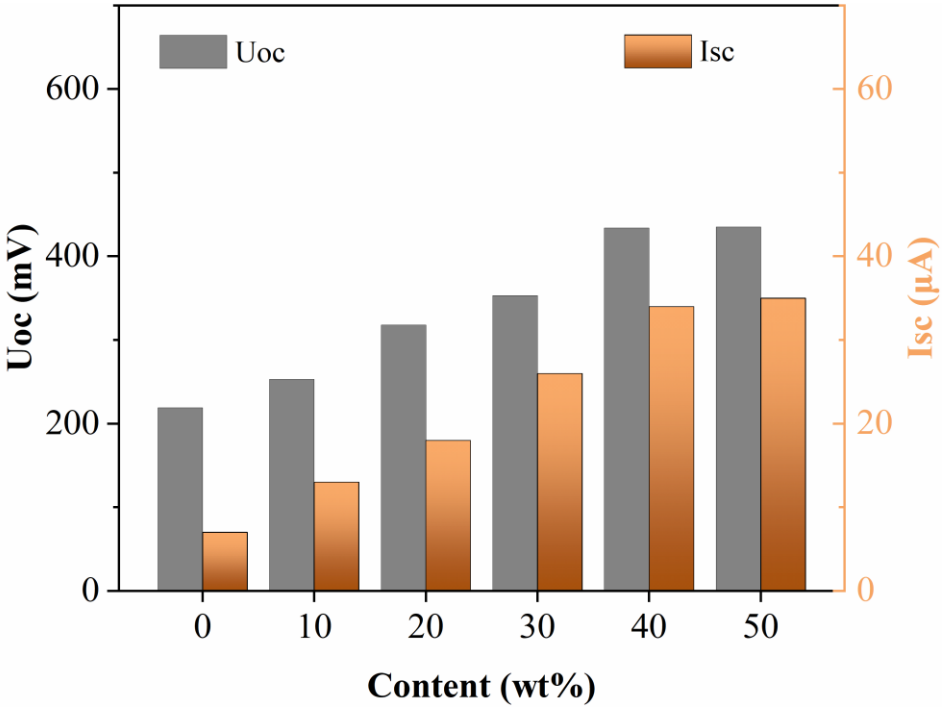

Fig. S21 Uoc and Isc of SWNT/PVA/CNF aerogels with different SWNT contents

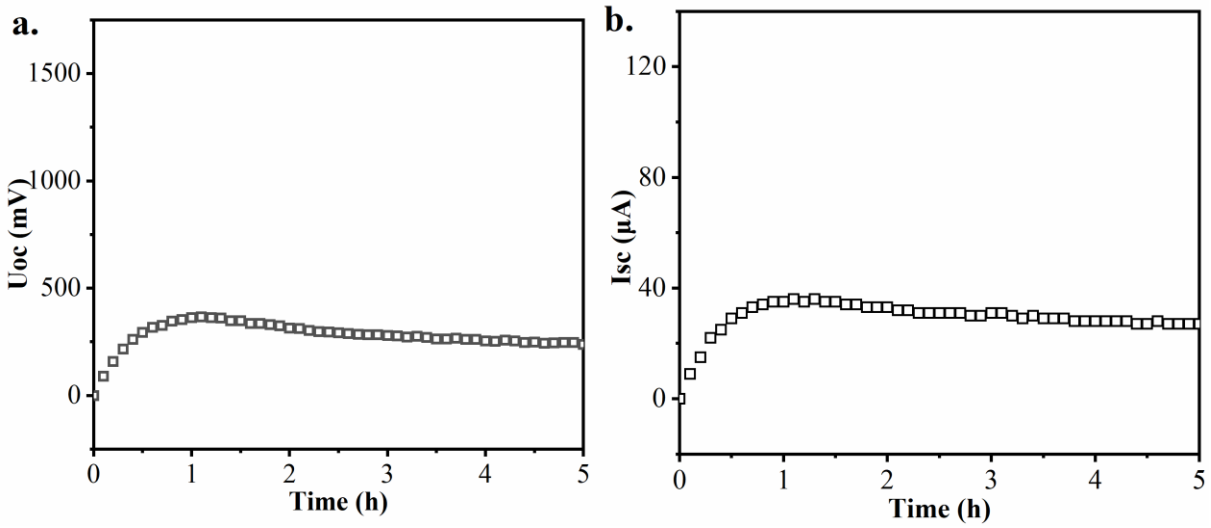

Fig. S22 a. Uoc-time and b. Isc-time curves of SWNT/PVA/CNF aerogels with 40 wt.% SWNT contents

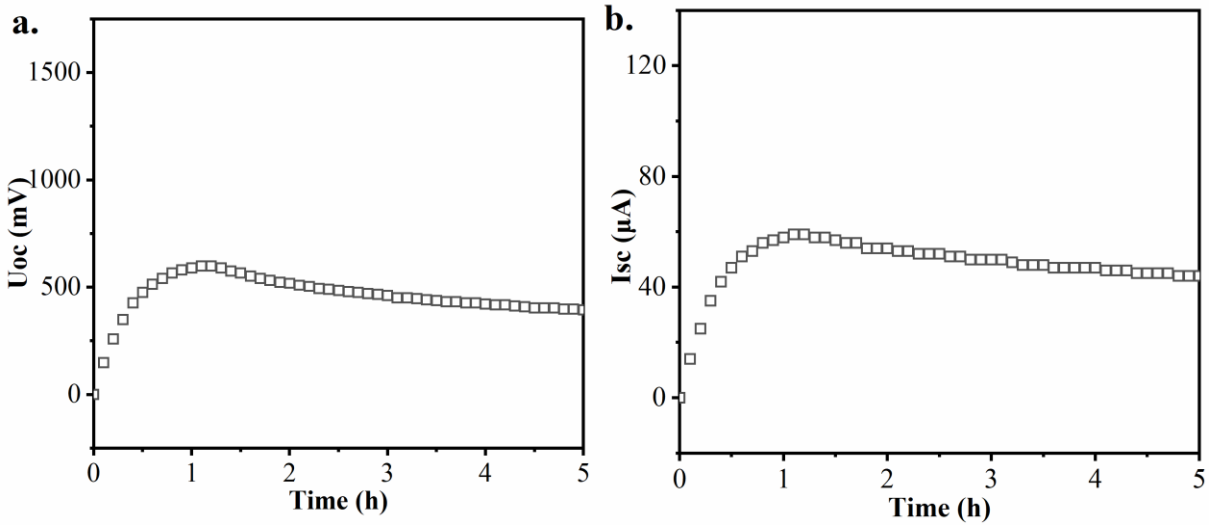

Fig. S23 a. Uoc-time and b. Isc-time curves of SWNT@PVA/CNF aerogels with 40 wt.% SWNT contents

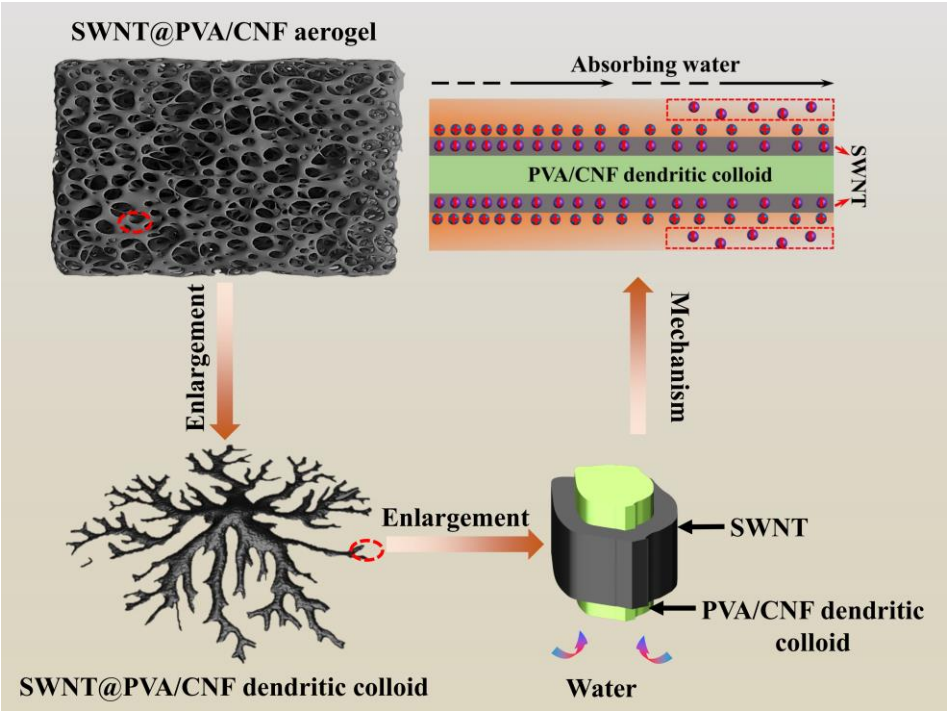

Fig. S24 The working mechanism of moisture-electric energy conversion of SWNT@PVA/CNF aerogels

4.5.2. Thickness dependence

Water flow rate is primarily responsible for Uoc of MEGs, and the greater the flow rate, the greater the Uoc. Initially, as thickness increased, the water absorption of aerogels grew, the weight of water flowing through per unit area grew, and the direct interaction between water and fillers grew. MEGs exhibit a linear increase in Uoc with increasing thickness in a similar manner to multiple commercial batteries connected in series (Fig. S25). Due to the effect of gravitational potential energy, as the thickness of MEGs increases, the transport of water from the bottom to the upper part of MEGs becomes more difficult, and the flow rate of water per unit area decreases, resulting in a gradual decrease in the Uoc of MEGs with an increase in thickness. In summary, when the thickness of the aerogel is 15 mm, the Uoc of MEGs is the highest.

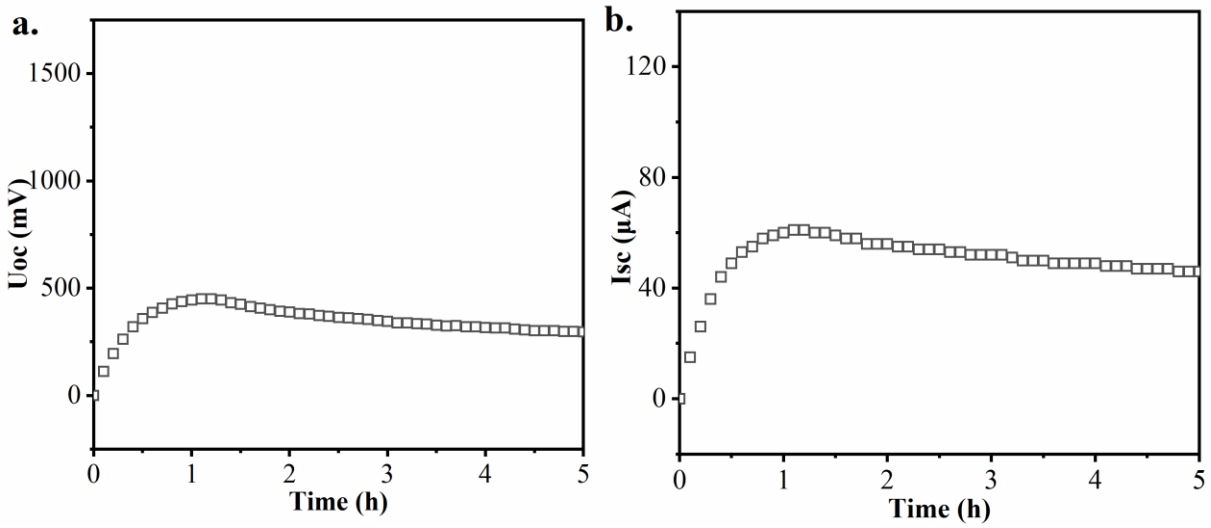

Fig. S25 a. Uoc-time and b. Isc-time curves of SWNT@PVA/CNF aerogels with a thickness of 10 mm

4.5.3. Area dependence

In MEGs, the Isc is determined primarily by the flow rate of water per unit thickness. With an increase in radius, the area of the airgel increases, the flow rate of water per unit thickness increases, and the interaction between the filler and water increases. When Uoc is almost constant, the Isc of MEGs increases in a similar way to parallel connection of multiple commercial batteries. Although the test results show that increasing the radius does help to increase the Isc of MEGs, the power density of MEGs does not continue to increase as the radius increases. From Table S4, when the radius of aerogel is 15 mm, the power density of MEGs is the highest (5.60 $\mu W \cdot cm^{-2}$). Additionally, as the radius increases, the difficulty of airgel preparation increases and the likelihood of collapse during freeze-drying increases. It was determined that the aerogel's radius was 15 millimeters based on the power density and the preparation of the aerogel.

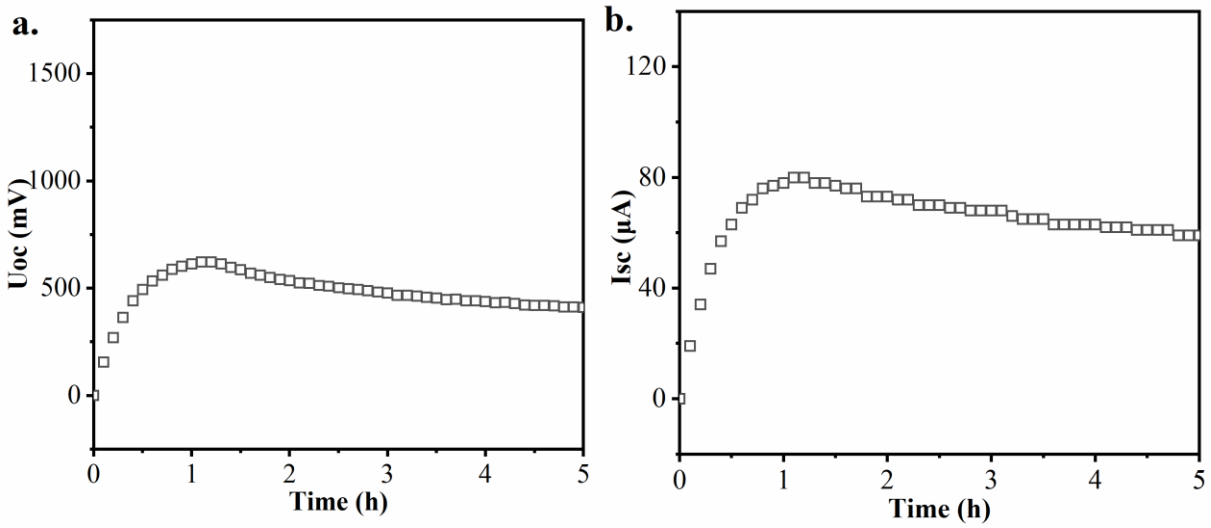

Fig. S26 a. Uoc-time and b. Isc-time curves of SWNT@PVA/CNF aerogels with a radius of 20 mm

Table S4. The area and power density of SWNT@PVA/CNF aerogels with different radius

Radius (mm)	Aera (cm^2)	Isc (μA)	Power Density ($\mu W \cdot cm^{-2}$)
5	0.785	5	3.29
10	3.14	18	4.09
15	7.065	61	5.60
20	12.56	82	4.25

4.5.4. Density dependence

In MEGs, a change in density has an adverse effect on the output performance due to the effect on the weight and water absorption of the filler. When the filler content remains unchanged, the weight of the filler inside the airgel increases as the density increases, and the probability of contact between water and the filler increases, thus improving the interface interaction. Meanwhile, with increasing density, the water absorption of aerogels decreases, which is detrimental to the performance of MEGs (Fig. S27). When the density of the aerogel is 20 $mg \cdot cm^{-3}$, the competition between the two leads to the best Uoc and Isc of MEGs (Fig. S28-29). In addition, from Fig. S30, density affects the airgel's moisture permeability by modifying the size of the pores. As density decreases, pore size increases, which hinders

capillary force in the microporous structure, and the water transport speed is slower (Fig. S31). The higher the density, the smaller the pore size of the airgel, the stronger the van der Waals force between the water and the polymer matrix, and the slower the rate of water flow.

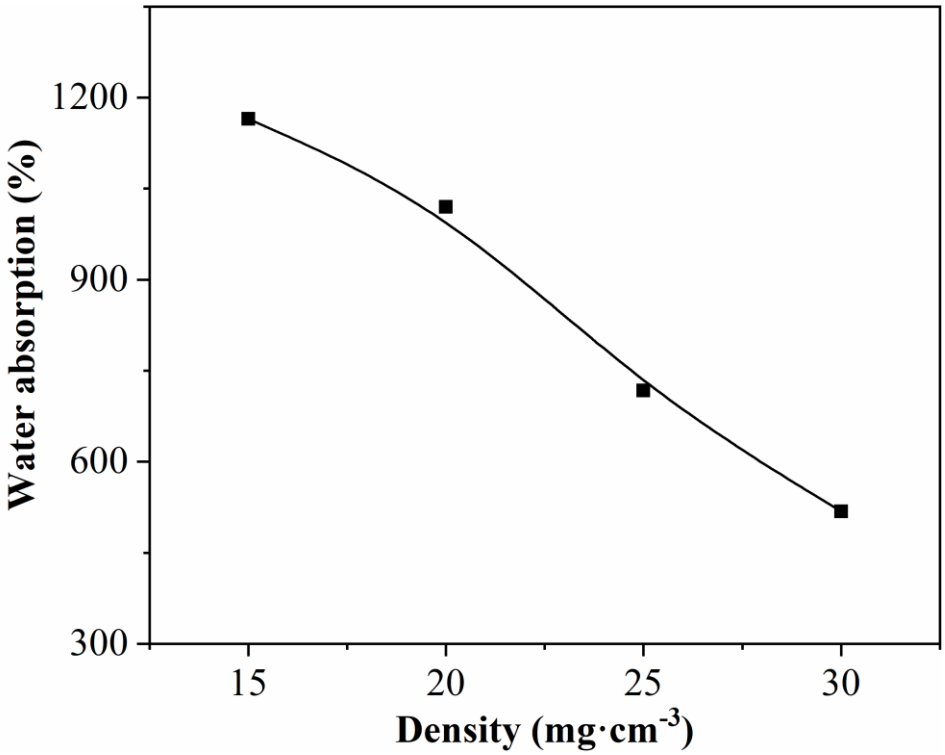

Fig. S27 Water absorption of SWNT@PVA/CNF aerogels with different density

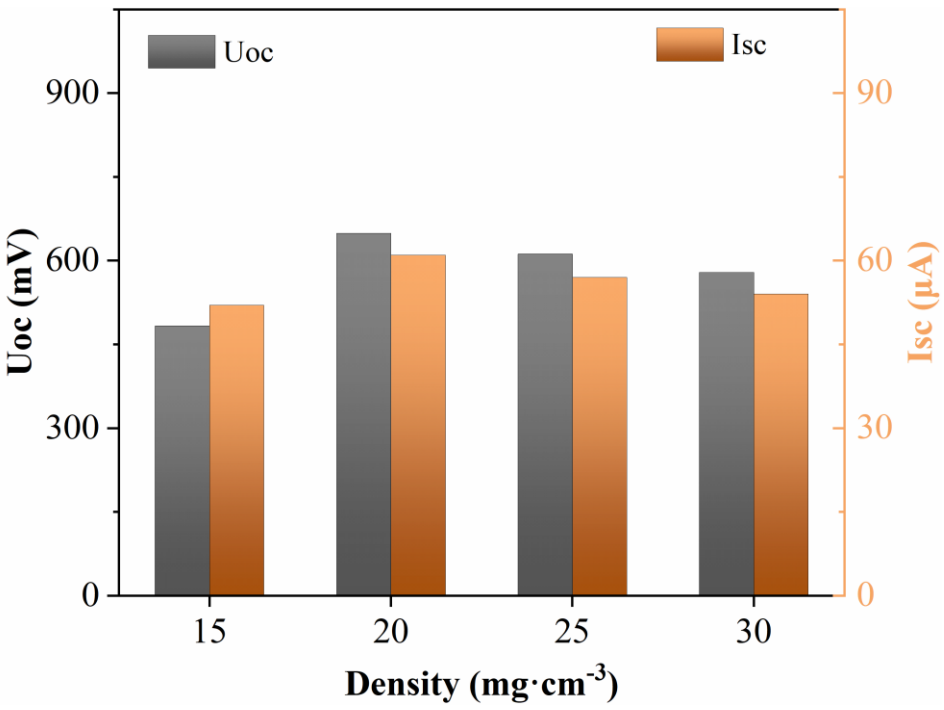

Fig. S28 Uoc and Isc of SWNT@PVA/CNF aerogels with different density

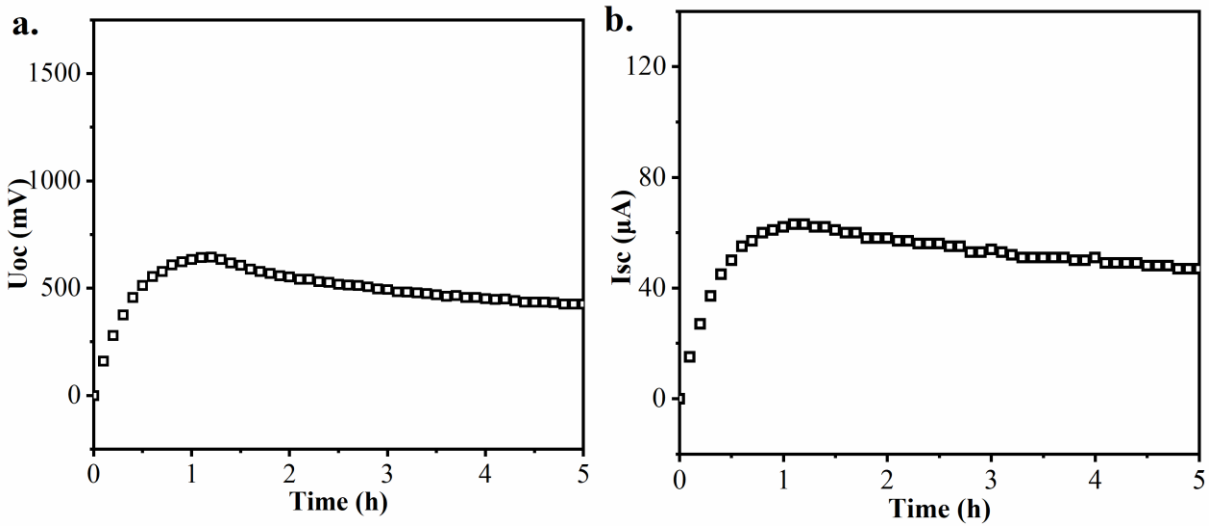

Fig. S29 a. Uoc-time and b. Isc-time curves of SWNT@PVA/CNF aerogels with a density of 20 mg·cm^{-3}

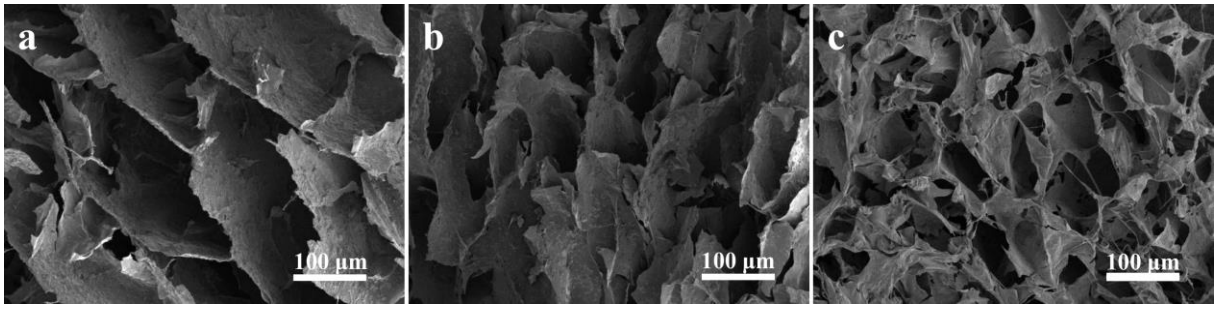

Fig. 30 FESEM of SWNT@PVA/CNF aerogels with different densities: a. 15, b. 20 and, c. 30 mg·cm^{-3}

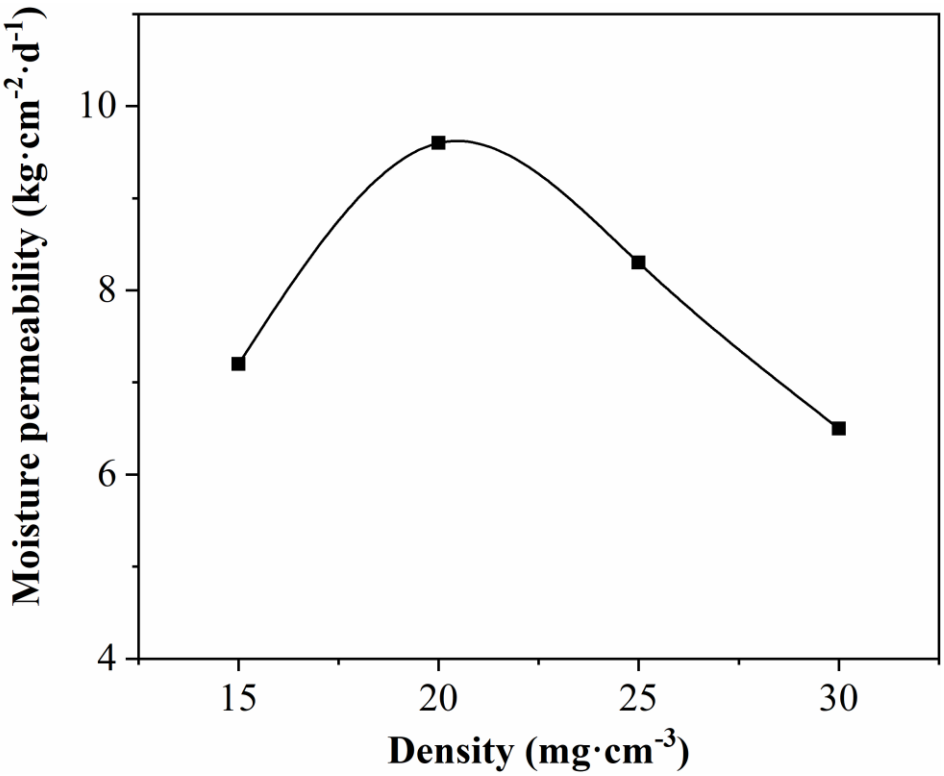

Fig. S31 Moisture permeability of SWNT@PVA/CNF aerogels with different density

4.5.5. Comparison of literatures

Table S5 Comparison of MEGs in this work with literature

Ref	Active material	Matrix	Structure	Methodology	Ion gradient	Hydrophilicity gradient	Power density ($\mu wh \cdot cm^{-2}$)	Energy density ($\mu w \cdot cm^{-2}$)
[9]	GO	PVA	Aerogel	Freeze drying	√	×	23.5	7.73
[16]	GO	PVA	Aerogel	Freeze drying	√	×	18.75	42.36
[39]	PEDOT: PSS	PSSA	Hydrogel	Cross-linking	√	×	26.55	81.79
[40]	CB	PVA	Hydrogel	Cross-linking	×	√	15.03	45.08
[41]	Phytic acid	PVA	Hydrogel	Crosslinking	√	×	10.69	15.73
[42]	MOF/GO	ILs	Film	Cast forming	√	×	12	2.00
[43]	Protein nanofibrils		Film	Coating	×	√	9.29	7.55
[44]	Cellulose/SDBS		Fabric	Electrospinning	√	×	11.5	24.22
[45]	GO	PU	Foam	Coating	√	×	19.87	24.64

[46]	CNTs	Cellulose	Paper	Coating	×	√	14	3.37
This Work	SWNTs	PVA/CNF/CS	Aerogel	Freeze drying	√	√	**32.59**	**165.23**

4.5.6. Cycling stability

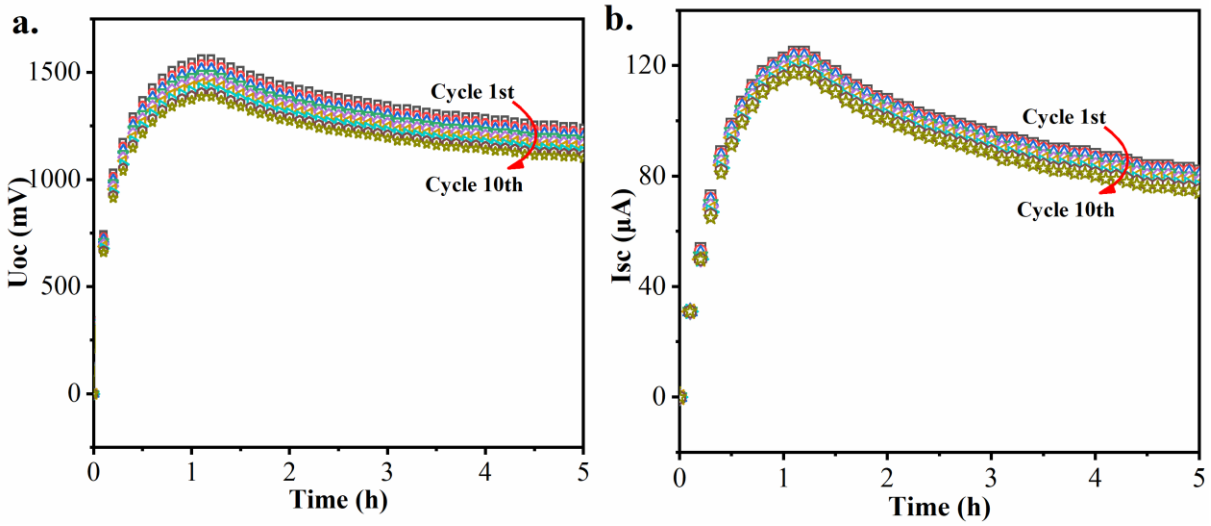

Fig. S32 a. Uoc and b. Isc of NSC@CCP aerogels with different cycles.

4.5.7. Electrode dependence

A porous nickel electrode and a porous silver electrode were selected as electrodes for further study of MEG performance, as shown in Fig. S33[S1]. Whenever the work function of a metal is less than the work function of a carbon nanotube, the conduction band of the metal contacts the carbon nanotube, and electrons serve as the carriers. In contrast, the valence band of a metal is in contact with a carbon nanotube if its work function exceeds that of a carbon nanotube, and the carrier is a hole in the valence band is greater. It is found that the work functions of Ag and Ni electrodes are 4.26 and 4.6 eV, respectively, which are lower than those of SWNT (4.83 eV). Consequently, both Ag/SWNT and Ni/SWNT exhibit Schottky diode characteristics, in which electrons flow from metal electrodes to SWNTs. There are opposite Schottky junctions on two Ag or Ni electrodes, which severely weaken the charge diffusion (Fig. S33a-b and d). Generally, as is shown in Fig. S34-35, MEGs operate at about 1.5 V and

130 μA when Ag or Ni is used as the electrode (including Ag-Ag, Ni-Ni, Ag-Ni). Pt electrodes show a higher work function than SWNT electrodes, indicating an ohmic contact (Fig. S33c). From Fig. S34-35, due to a lack of Schottky junction between the two Pt electrodes, electrons flow from the semiconductor to the metal, resulting in the recombination of positive and negative charges and the reduction of Uoc (≈1.37 V) and Isc (≈112 μA). As is shown in Fig. S4-35, MEGs with Ag-Pt or Ni-Pt alternating electrodes have Uoc and Isc values close to 1.73 V and 127 μA, respectively. Ag/SWNT or Ni/SWNT interfaces form a space charge region that prevents negatively charged electrons from flowing into the SWNT layer, thereby promoting charge separation in the entire SWNT (Fig. S33e-f).

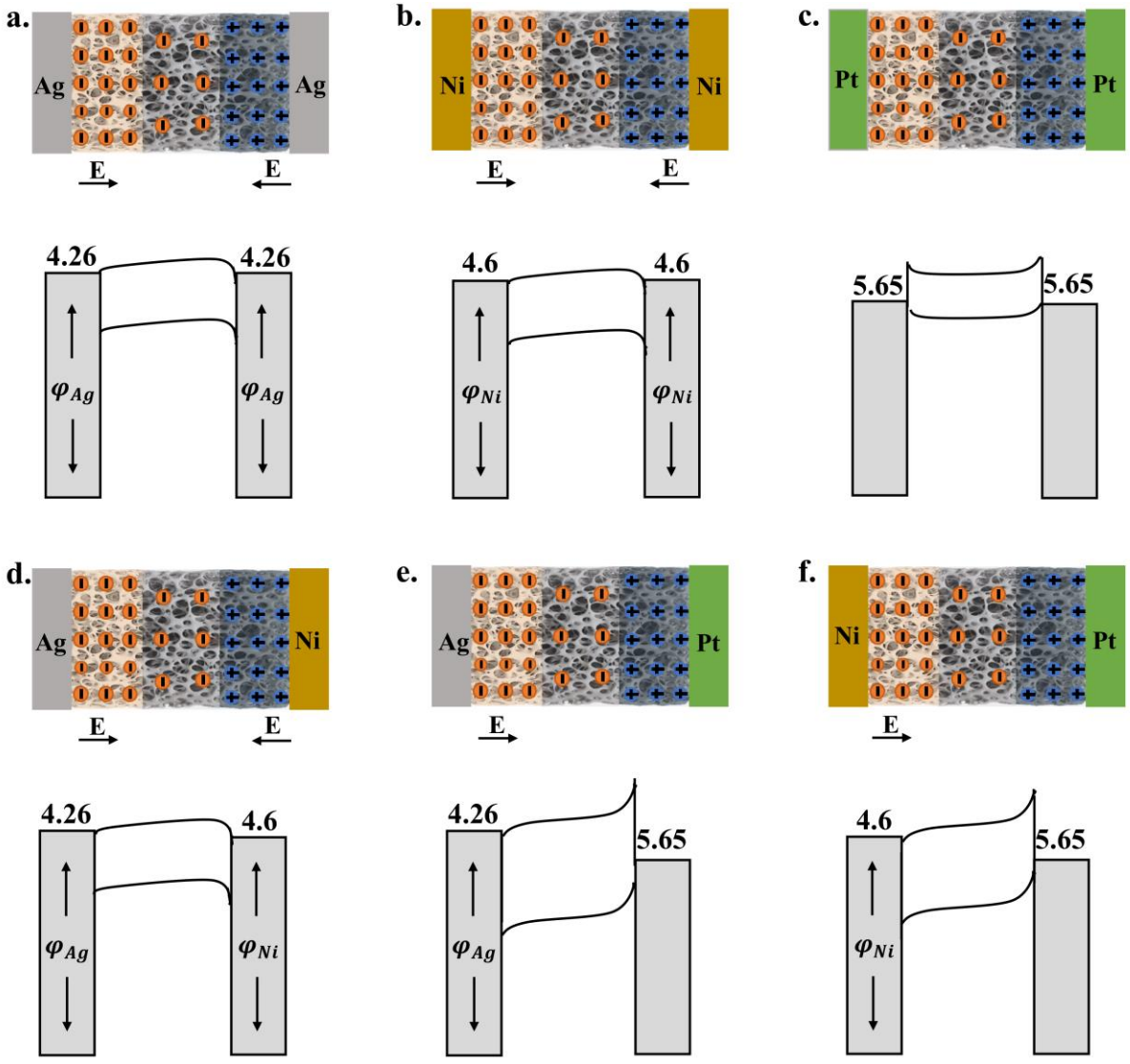

Fig. S33 Comparison of MEGs with different configurations. a–f Device structure (top) and energy band

diagram (bottom)

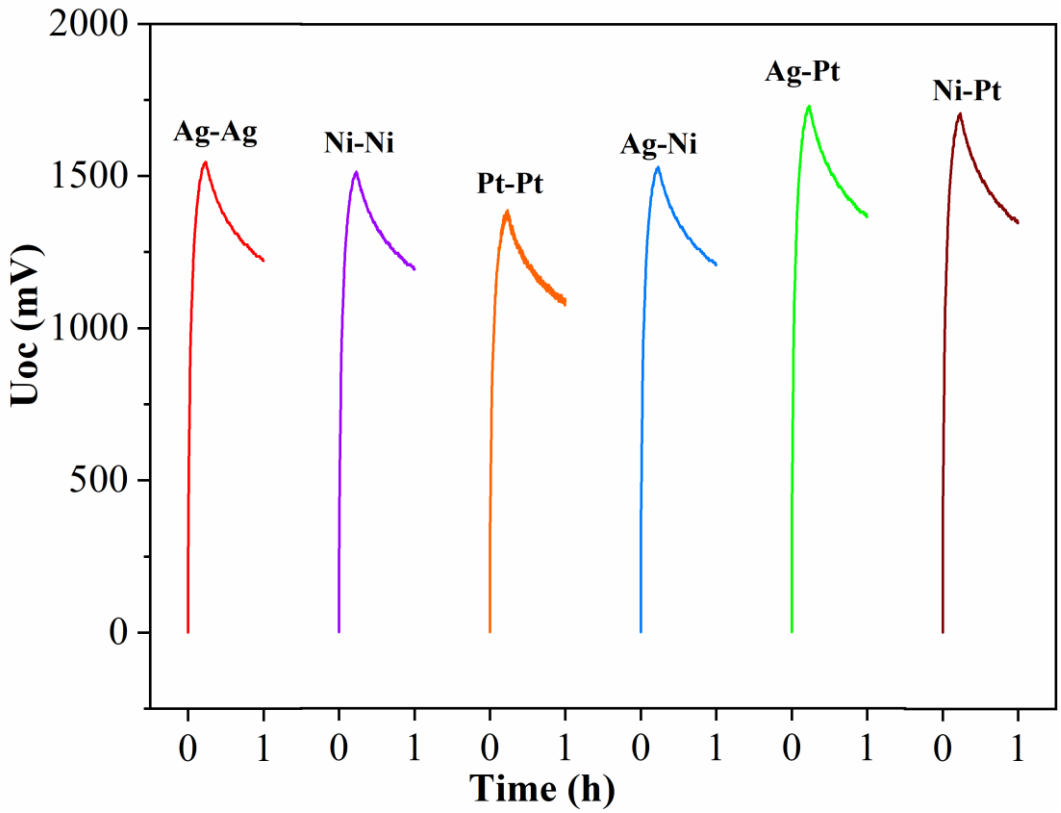

Fig. S34 Uoc-time curves of the above three MEGs with different device configuration

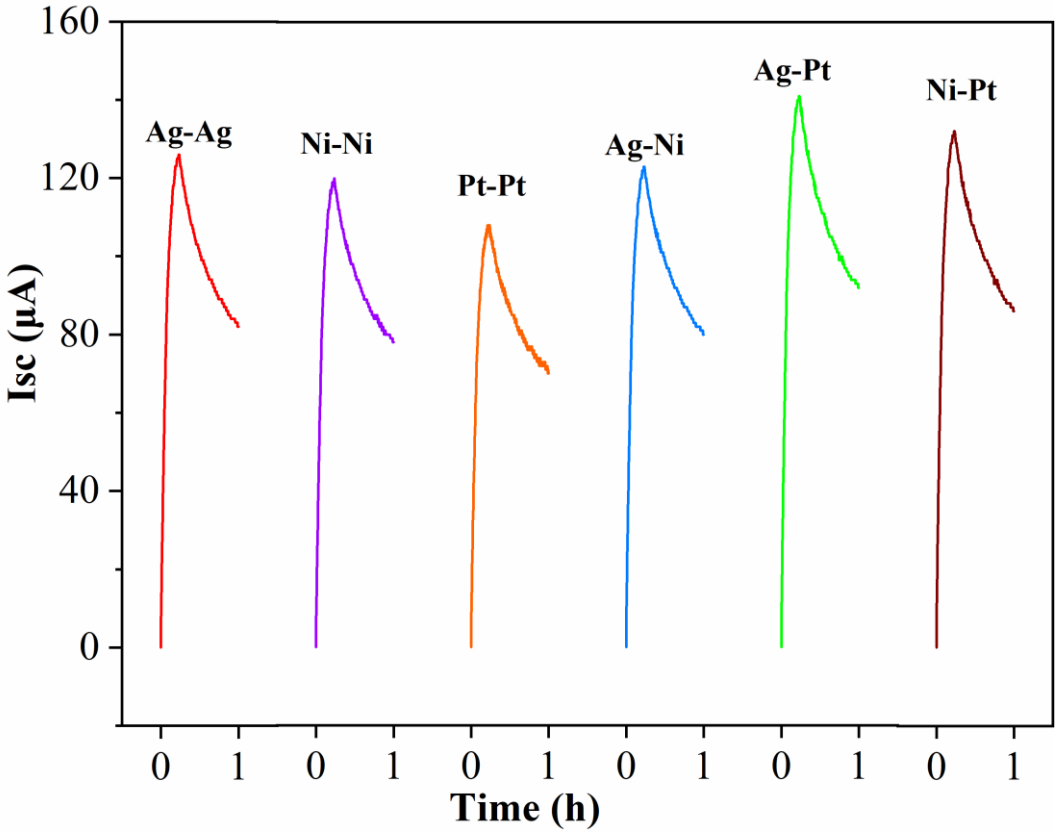

Fig. S35 Isc-time curves of the above three MEGs with different device configuration

4.5.8. Density Functional Theory (DFT) calculations

The binding energy and charge transfer of SWCNTs, CSWNT, and NSWNT and water molecule are studied by the DFT-based Vienna ab initio simulation package (VASP). Exchange-correlation energy is described by general gradient approximation with the projector augmented wave method and Perdew–Burke–Ernzerhof functional[S2,3]. The projected-augmented wave (PAW) method was used to describe the electron–ion interactions, and for valence electrons, a plane-wave basis set was employed. The generalized gradient approximation method is known as GGA-PBE was used for the exchange–correlation function. A cut-off energy of 500 eV was imposed for the plane-wave basis set, and G-point sampling was used for the Brillouin zone integration. To nullify the interactions between periodic images along the axis perpendicular to the surface, all slabs were separated by 20 Å along this direction perpendicular. The initial structures were generated by Materials Studio, and the initial geometries were further relaxed

via DFT simulations. The kinetic energy cutoff is set at 600 eV and the energy and force convergence was set at 10^{-8} eV and 10^{-3} eV/Å. The projector augmented wave potentials are used with a kinetic energy cutoff of 500 eV—a 5 × 5 k mesh sampled Brillouin zone integration (Fig. S36-41). The system is simulated with a periodic boundary condition by placing one or four water molecules on the surface of a 4 × 14 supercell of the SWNT, spaced by 20 Å along the average direction. CSWNT and NSWNT are constructed by GaussView 6.0. Dipole correction is considered to exclude the artificial dipole-dipole interaction between adjacent images. The geometry is fully relaxed without any constraint by using the conjugate gradient method until the force on each atom was less than 0.01 eV·Å^{-1}. The adsorption energy for hydrated ions adsorbed on graphene was calculated using $E_a = E_g + E_{hi} - E_{system}$, where E_g, E_{hi} and E_{system} are the energies of SWNT, a hydrated ion and the combined system, respectively.

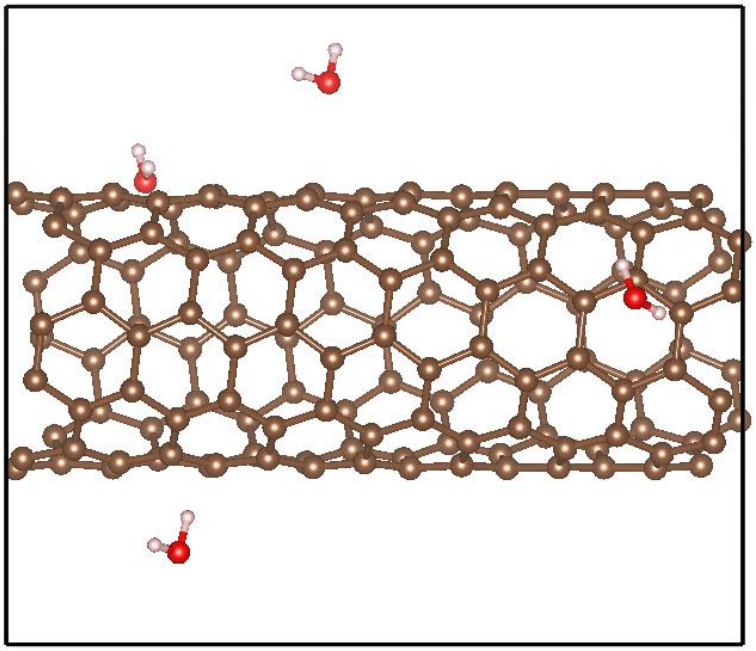

Fig. S36 Models for DFT calculation of four water molecules adsorbed on SWNT

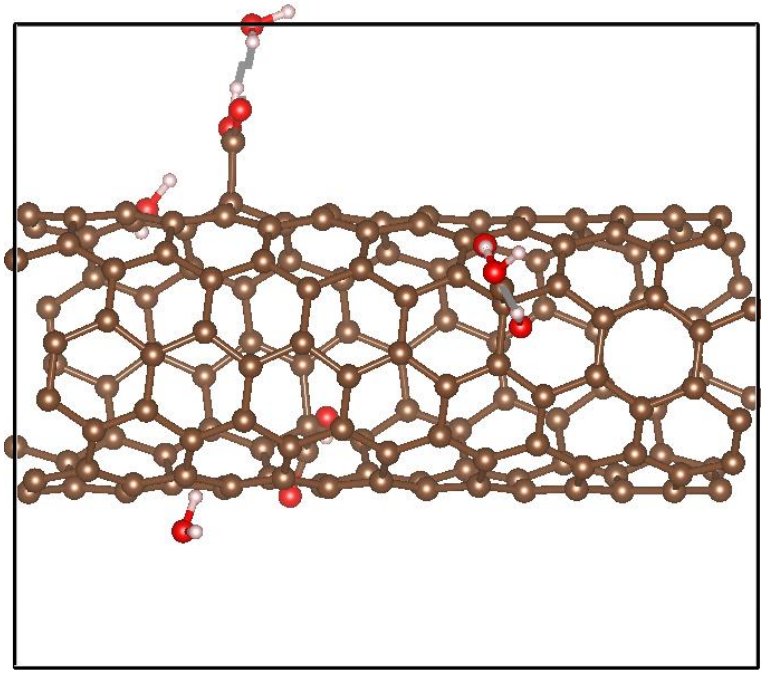

Fig. S37 Models for DFT calculation of four water molecules adsorbed on CSWNT

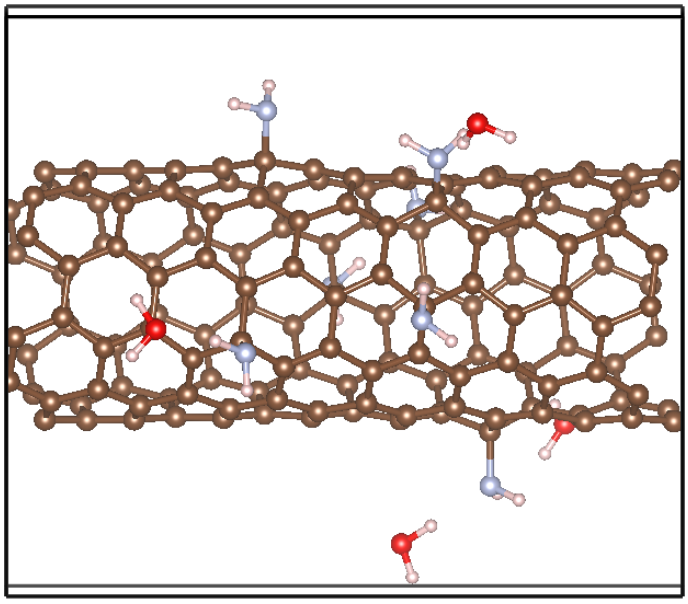

Fig. S38 Models for DFT calculation of four water molecules adsorbed on NSWNT

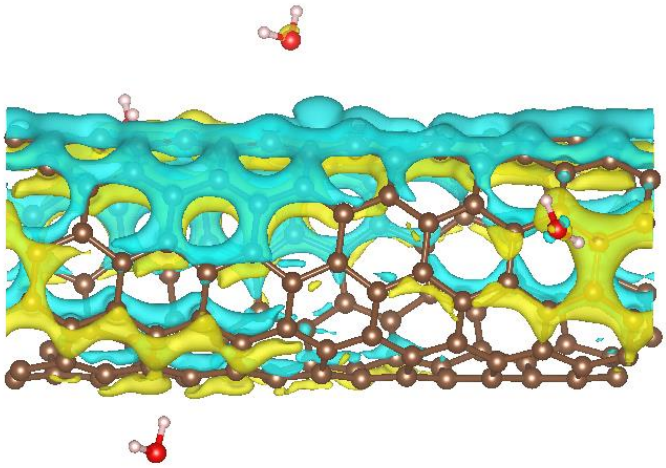

Fig. S39 Charge redistribution of SWNT upon adsorption of four water molecules

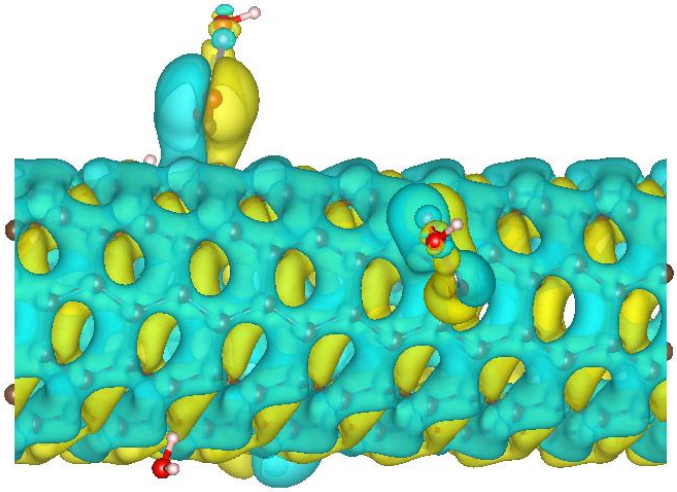

Fig. S40 Charge redistribution of CSWNT upon adsorption of four water molecules

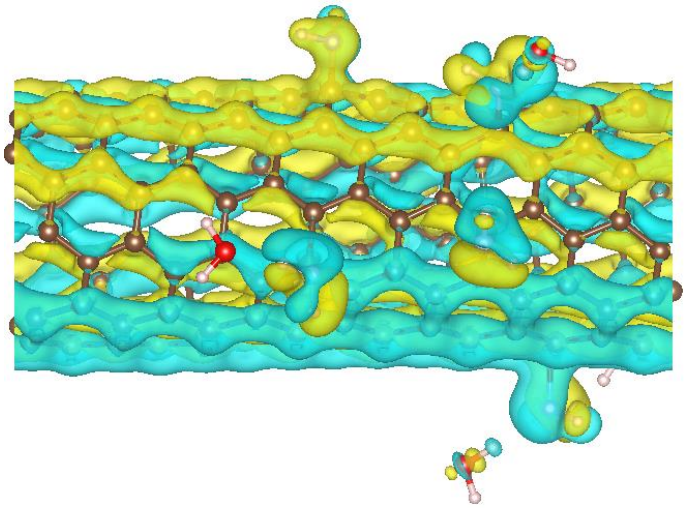

Fig. S41 Charge redistribution of NSWNT upon adsorption of four water molecules

4.5.9. KPFM

A scanning KPFM system (SKP5050, KP technology) was used to characterize the surface potentials of the hygroscopic, medial and evaporation layers before and after moisturizing. A highly oriented pyrolytic graphite reference sample (ScanSens GmbH) was used to calibrate the system.

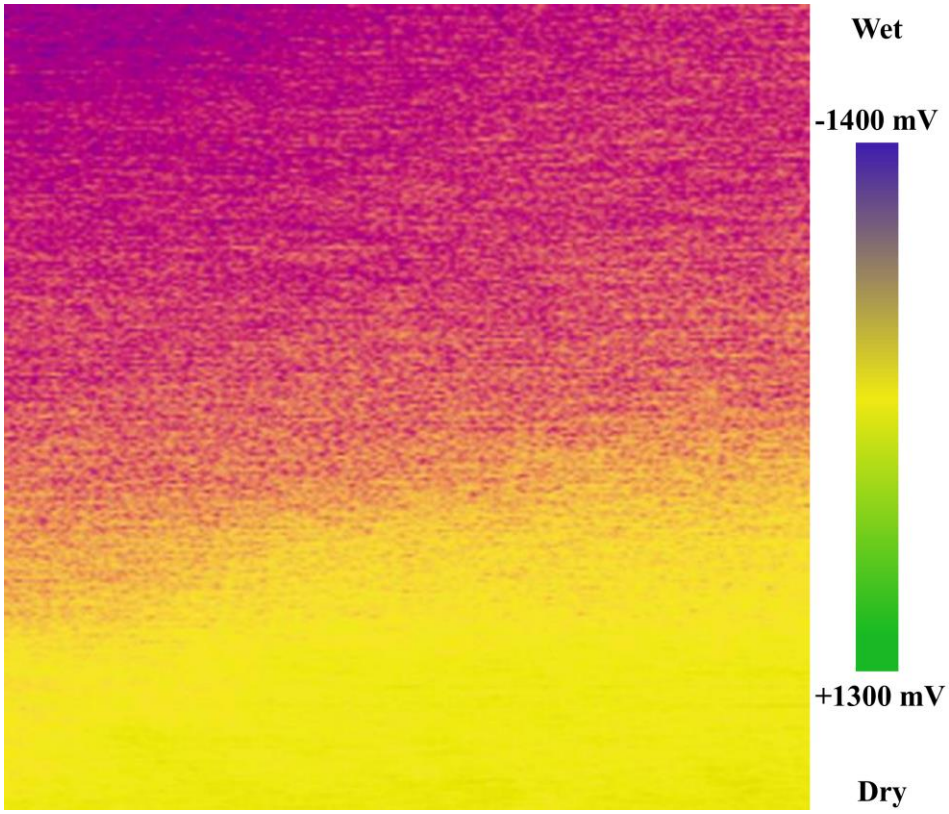

Fig. S42 Relative surface potentials of the medial layer of NSC@CCP aerogel under dry and wet

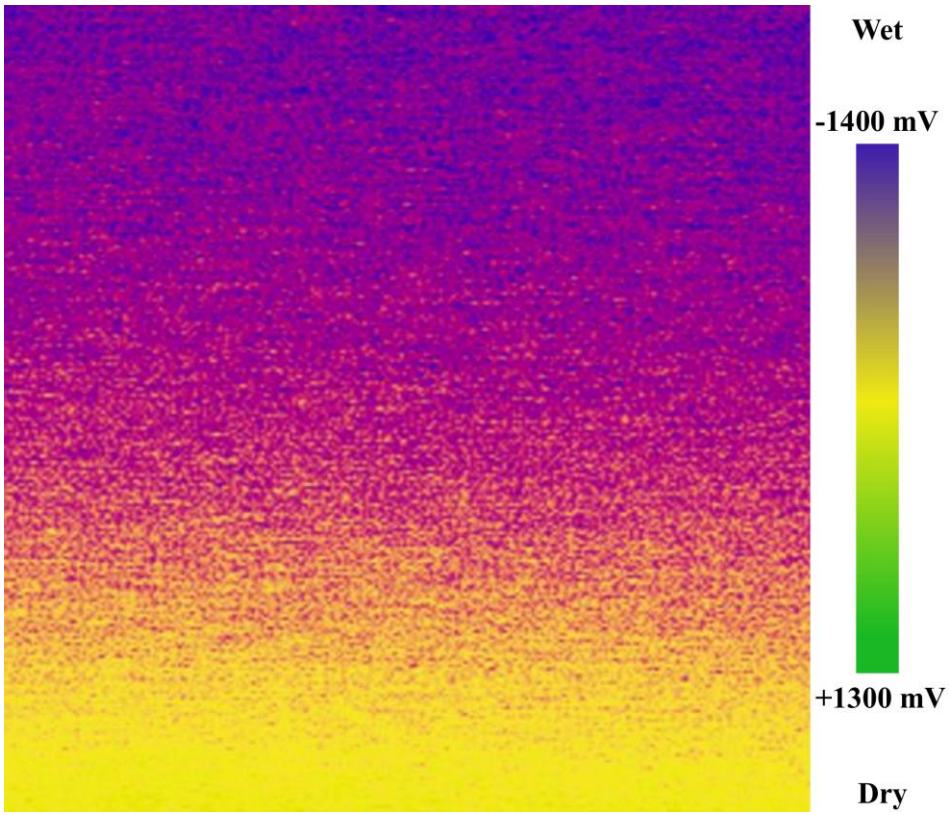

Fig. S43 Relative surface potentials of the hygroscopic layer of NSC@CCP aerogel under dry and wet

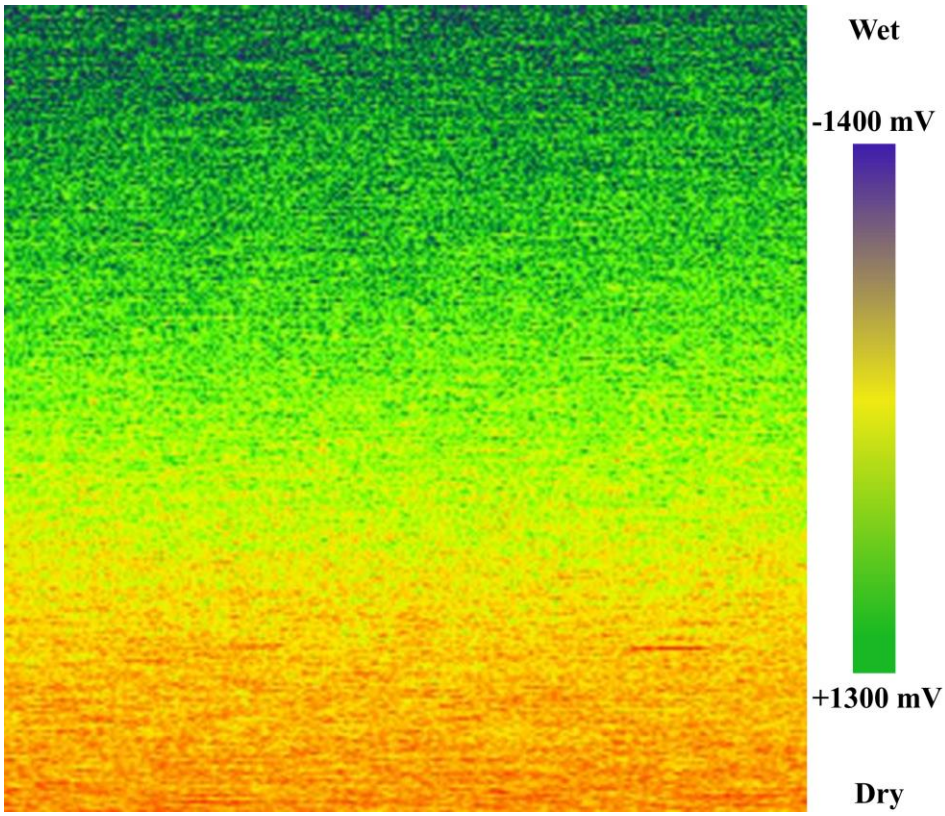

Fig. S44 Relative surface potentials of the evaporation layer of NSC@CCP aerogel under dry and wet

4.5.10. Ion density gradient dependence

The zeta potentials of the hygroscopic, medial and evaporative layers were measured using a solid surface Zeta potential tester (SurPASS 3, Austria) by flow potential method at pH = 7.

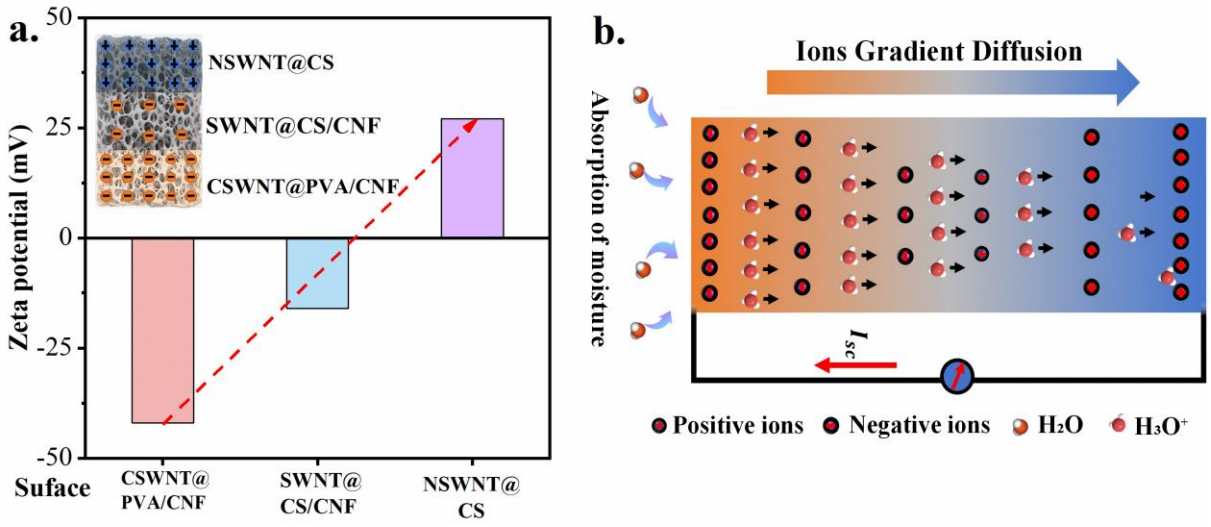

Fig.S45 a. Zeta potential of the hygroscopic, medial and evaporative layer; b. Schematic illustration of the

working mechanism of the MEGs

4.5.11. Hydrophilicity gradient dependence

4.5.11.1. Mass change

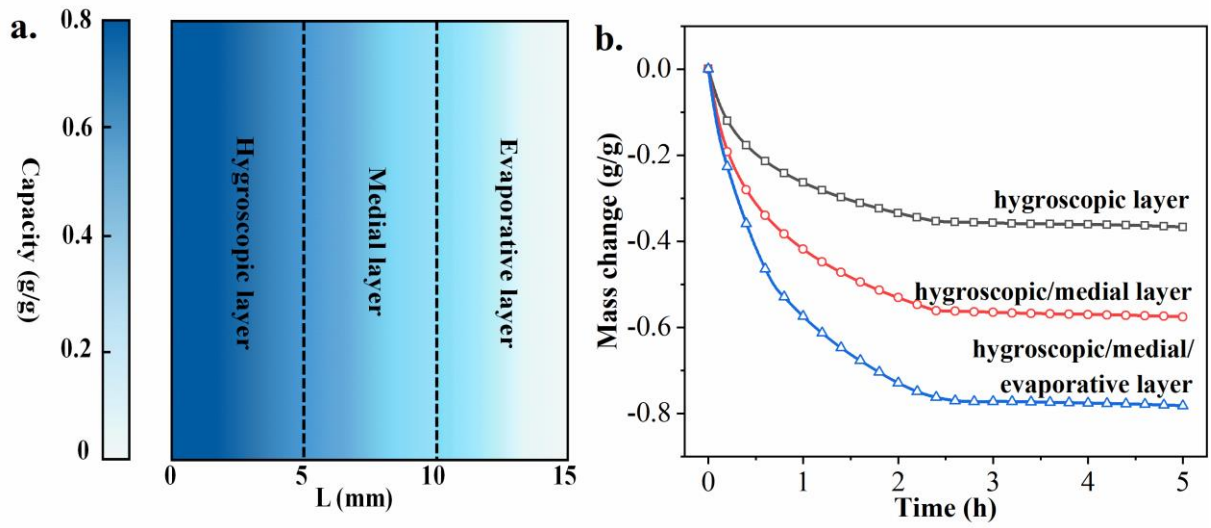

Fig. S46 a. Water content map of the MEGs after moisture adsorption in 60% RH for over 24 h. The water content map was depicted by gravimetrically analyzing water absorbed by each layer. b Mass change in the hygroscopic layer, hygroscopic layer/medial layer and hygroscopic layer/medial/evaporative layer versus time under one-sun illumination.

4.5.11.2. COMSOL simulations

Numerical simulations of water transport in aerogel were conducted by COMSOL Multiphysics 5.3. The geometry was established under the same size and similar shape as the aerogel. The mass transfer process in the aerogel includes two-phase flows, liquid phase transport, and vapor phase transport[S4]. For two-phase flows, the aerogel can be considered as a porous solid matrix, where the saturation variables of moist air (S_g) and water (S_l) flow in the porous gel fulfill the following Equation S1,

$$S_g + S_l = 1 \qquad \text{Eq. S1}$$

The Brinkman Equation S2 was used to calculate the flow field u_g and pressure

distribution p_g of moist air in the porous medium,

$$-\nabla p_g + \nabla \frac{\mu}{\varepsilon}\left(\nabla u_g + \nabla u_g^T\right) - \frac{\mu}{\kappa} u_g = 0 \qquad \text{Eq. S2}$$

where p_g is the pressure of moisture air, u_g is Darcy's velocity field, μ is the dynamic viscosity of the fluid, ε is the porosity, and κ is the permeability of the medium.

The liquid water transport velocity of porous aerogel is simulated by solving the combination of Darcy's Law and capillary effect,

$$u_l = -\frac{\kappa_l}{\mu_l} \nabla p_l \qquad \text{Eq. S3}$$

Where κ_l, μ_l and ∇p_l are the permeability, viscosity, and pressure gradient of the liquid phase within the aerogel, respectively. The mass transport of the liquid phase inside the porous domain can be written as follows:

$$R = -\frac{\partial c}{\partial t} \nabla \cdot J \qquad \text{Eq. S4}$$

where J represents the diffusion flux of water, and R represents the mass of the evaporation. The water vapor transfer velocity could be defined as:[S5]

$$u = \frac{u_g}{S_g \varepsilon} - \frac{\rho_g}{M_g^2} D_{eff} \nabla \left(\frac{M_g}{\rho_g}\right) \qquad \text{Eq. S5}$$

where M_g and ρ_g refer to the mass and density of the moist air, respectively, M_a is the mass of air, D_{eff} is the effective diffusivity for two components and is defined by Millington and Quirk equation:

$$D_{eff} = D_{va} \varepsilon^{4/3} S_g^{10/} \qquad \text{Eq. S6}$$

where the D_{eff} is the vapor-air diffusivity with the value of 2.6×10^{-5} m^2 s^{-1}.

Considering the water confinement of the polymeric network and the convection of the air, the heat transfer near the surface could be described by the equation given below:

$$E = \rho C_{p,tot} \frac{\partial T}{\partial t} + \rho C_{p,tot} u \cdot \nabla T + \nabla [\kappa_{tot} \nabla T] \qquad \text{Eq. S7}$$

where E represents the thermal energy input from the optical-thermal conversion. ρ, $C_{p,tot}$ and κ_{tot} are the total density, heat capacity, and thermal conductivity of moist air and liquid phase, respectively.

The latent heat source within the aerogel is set to be Q_{evap},

$$Q_{evap} = -H_{evap} \cdot m_{evap} \qquad \text{Eq. S8}$$

where H_{evap} is the latent heat of evaporation, and m_{evap} is the evaporation flux at the aerogel top surface.

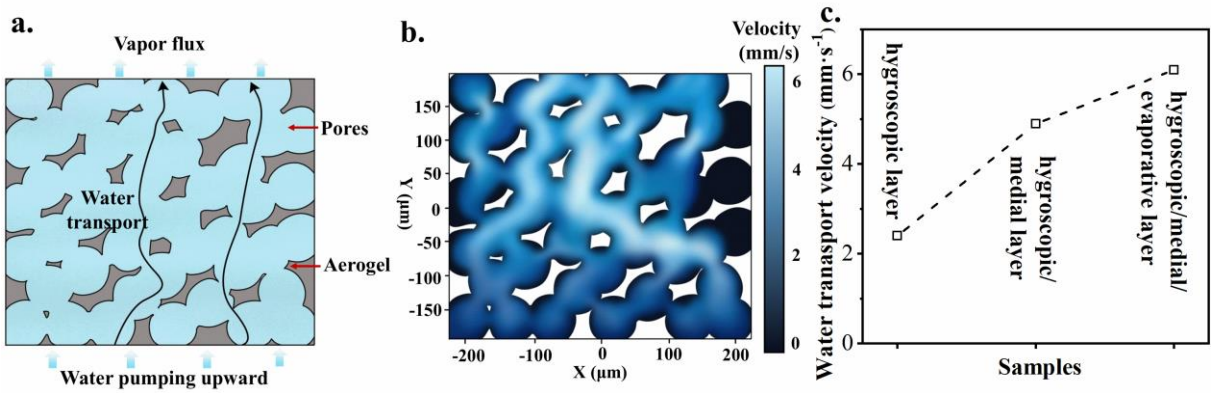

Fig. S47 a. Schematic of the COMSOL model of aerogel, b. Simulated water transport velocity mapping and low-tortuosity water pathways in aerogel, c. Calculated water transport velocity of aerogel via COMSOL.

4.5.12. Energy conversion efficiency.

4.5.12.1. Calculation of input energy.

Since there is no extra energy in the MEET system, Gibbs free energy (ΔG) is the sole energy source in the energy conversion process and defines the maximum power output.

$$\Delta G = u_1 - \mu_2 \approx RT\, ln \frac{C_0}{C_0 - \Delta C} \qquad \text{Eq. S9}$$

where R, T and C_0 are ideal gas constant, Kelvin temperature, and relative humidity of the inserted water end in MEGs[S6-8]. Since the air humidity is tested as 40 % and the ΔC is assumed to be 60%, C_0 should be 100 %. As a result, we get ΔG ≈ -2.20 KJ·mol^{-1} at 293 K. Based on the weight change of foam before, and after absorbing water, the weight of absorbed water (≈ 4.10 g) is obtained. The calculated energy input of one cycle of MEGs is 70.79 **μW**·cm^{-2}.

4.5.12.2. Calculation of internal energy conversion efficiency.

The power output (W_{MEGs}) of MEGs can be calculated as: $W_{MEGs} = \int I_{sc}(t) \cdot U_{oc}(t)\, d(t)$ where I_{sc}, $U_{oc}(t)$ and t is the short-circuit current density, open-circuit voltage, and cycle time. The calculation results showed ca. 32.59 **μW**·cm$^{-2,}$ and the CPE harvesting efficiency is ca. 46.04%

5. Application

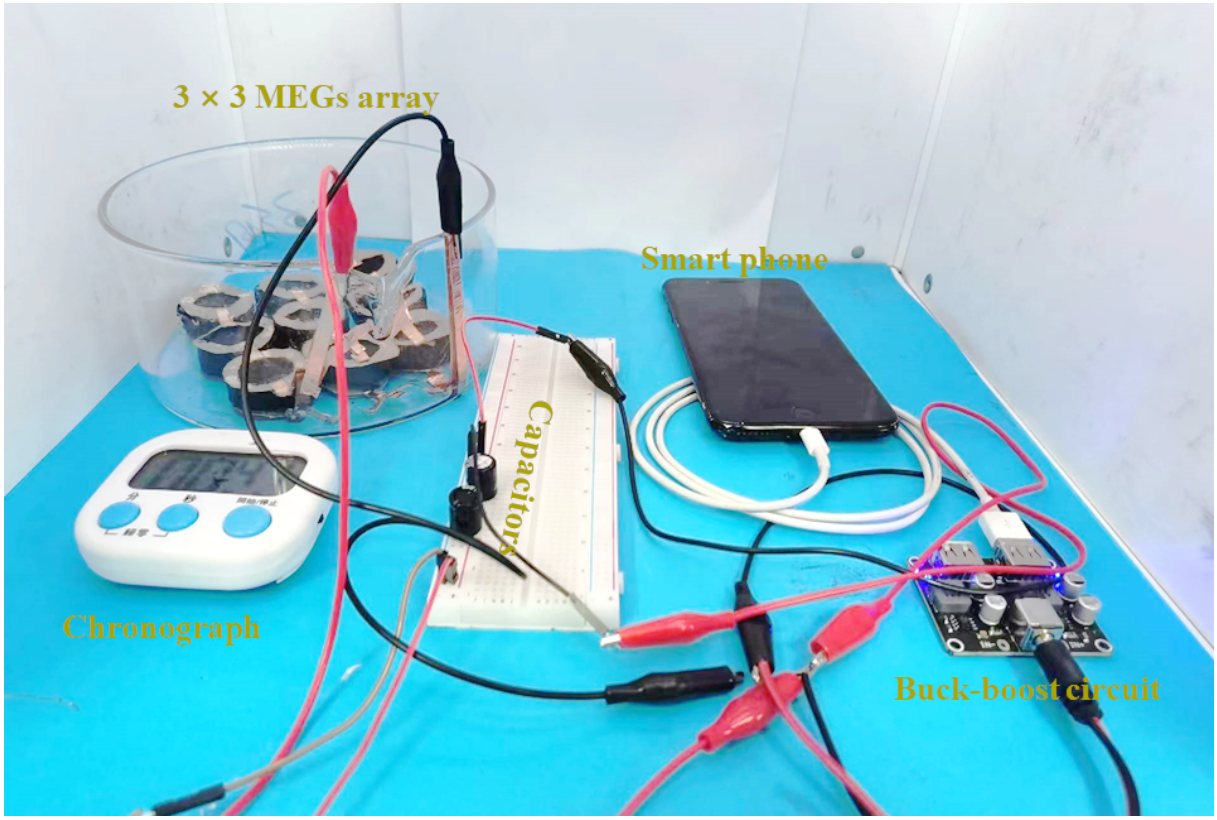

Fig. S48 Photograph of a working MEGs in combination with the power-management circuit to charge a smart phone.

6. Supporting References

S1 Y. Huang, H. Cheng, C. Yang, P. Zhang, Q. Liao, H. Yao, G. Shi and L. Qu, Nat. Commun., 2018, 9, 4166.

S2 C. Liu, S. Wang, X. Wang, J. Mao, Y. Chen, N. X. Fang and S. P. Feng, Energy Environ. Sci., 2022, 15, 2489–2498.

S3 J. Bae, T. G. Yun, B. L. Suh, J. Kim and I. D. Kim, Energy Environ. Sci., 2020, 13, 527–534.

S4 A. K. Datta, J. Food Eng., 2007, 80, 80–95.

S5 Y. Guo, L. S. Vasconcelos, N. Manohar, J. Geng, K. P. Johnston and G. Yu, Angew. Chemie, , DOI:10.1002/ange.202114074.

S6 Y. Zhang, T. Xiong, D. K. Nandakumar and S. C. Tan, Adv. Sci., , DOI:10.1002/advs.201903478.

S7 Y. Zhang, H. Zhang, T. Xiong, H. Qu, J. J. Koh, D. K. Nandakumar, J. Wang and S. C. Tan, Energy Environ. Sci., 2020, 13, 4891–4902.

S8 J. Mao, J. Iocozzia, J. Huang, K. Meng, Y. Lai and Z. Lin, Energy Environ. Sci., 2018, 11, 772–799.